Energy, exergy, economic and enviro-economic analysis and artificial neural network modeling of an air-cooled PVT collector with NACA 8412 airfoils

Çerçi, Kamil Neyfel

DOI
10.1016/j.applthermaleng.2025.126955

Publication date
2025

Document Version
Final published version

Published in
Applied Thermal Engineering

Applied Thermal Engineering 277 (2025) 126955

Contents lists available at ScienceDirect

Applied Thermal Engineering

journal homepage: www.elsevier.com/locate/apthermeng

Research Paper

Energy, exergy, economic and enviro-economic analysis and artificial neural network modeling of an air-cooled PVT collector with NACA 8412 airfoils

Kamil Neyfel Çerçi *

Tarsus University, Faculty of Engineering, Department of Mechanical Engineering, 33400, Tarsus, Mersin, Türkiye
Department of Process and Energy, Delft University of Technology, Leeghwaterstraat 39, 2628CB Delft, the Netherlands

ARTICLE INFO

Keywords:
Airfoil
Photovoltaic thermal
Energy
Exergy
Economic
Environmental
Artificial Neural Networks

ABSTRACT

This study numerically investigates the performance of an air-cooled photovoltaic thermal (PVT) collector integrated with NACA 8412 airfoils arranged at various positions in both flow (y) and transverse (x) directions, an application not previously explored in the literature. Using the finite element method, the effects of geometric parameters and a range of operational conditions, including airflow characteristics and environmental inputs, were evaluated. Artificial neural network (ANN) models were also developed to predict outlet air temperature, cell temperature, and pressure drop. Favorable energy and exergy performance was achieved with airfoil spacing of 50–70 mm (y-direction) and 35 mm (x-direction). To limit fan power consumption, the inlet air velocity should not exceed 5 m/s. The collector achieved efficiencies of 8.71–9.23 % (electrical), 50.34–70.85 % (thermal), 73.30–93.77 % (primary energy saving), and 10.23–10.69 % (exergy). The electricity production cost ranged from 0.158 to 0.668 $/kWh, and the exergoeconomic parameter varied between 4.10 and 17.55 kWh/$. Annual CO_2 mitigation reached up to 0.713 t (energy-based) and 0.275 t (exergy-based), depending on regional solar conditions. Two ANN model groups, one for single-output and one for multi-output predictions, were developed, both providing accurate and reliable results. This study offers a novel approach for enhancing and predicting PVT collector performance with airfoils.

1. Introduction

Energy is a fundamental driver of sustainability and progress in critical sectors that directly influence human life—such as industry, agriculture, education, and transportation [1,2]. With the continuous growth of the global population, the demand for energy across these sectors is rising steadily [3]. Globally, fossil fuels are widely used to meet this demand for both electricity and thermal energy production [4]. Fossil fuel reserves are inherently limited, and their combustion contributes to substantial environmental degradation, including ozone layer depletion, the greenhouse effect, and the accelerated melting of polar ice caps [5–7]. Addressing these environmental challenges requires reducing primary energy consumption, primarily through the integration of renewable energy sources such as solar, hydro, wind, and biomass, which have minimal environmental impact during their use. Among these, solar energy has gained considerable awareness due to its inexhaustible availability, renewable nature, and substantial sustainability benefits [8,9]. The primary approaches for utilizing solar energy are through photothermal and photovoltaic conversions. These are established and commercially available techniques for capturing solar energy to produce thermal and electrical energy.

Photovoltaic (PV) technology is the most advanced and widely adopted solar energy method due to its ability to generate clean, high-quality electricity with low cost, easy installation, minimal environmental impact, and autonomous operation [10,11]. In PV technology, over 80 % of the solar energy is transformed into heat, leading to a large amount of waste heat. If this waste heat is not removed from the PV panel through various types of collectors, it can damage the PV cells [12]. Considering this problem, photovoltaic/thermal (PVT) systems, an advanced concept of PV systems, have emerged as a promising technology that allows for the simultaneous generation of heat and electrical energy. These systems are a combination of a PV module that absorbs solar radiation and converts part of it into electricity, and a thermal collector that removes excess heat from the PV module to produce thermal energy [13]. Thus, PVT collectors enable the simultaneous

* Corresponding author at: Tarsus University, Faculty of Engineering, Department of Mechanical Engineering, 33400, Tarsus, Mersin, Türkiye.
E-mail address: kneyfelcerci@tarsus.edu.tr.

https://doi.org/10.1016/j.applthermaleng.2025.126955
Received 30 December 2024; Received in revised form 1 May 2025; Accepted 25 May 2025
Available online 26 May 2025

Nomenclature

a	Width of airfoil (mm)
AMC	Annual maintenance cost ($)
ANN	Artificial Neural Network
A_{PV}	Area of PV Surface (m^2)
ASV	Annual salvage value ($)
b	Length of airfoil (mm)
C	Energy conversion efficiency factor
$C_{e,n}$	Net electricity production cost ($/kWh)
c_p	Specific heat at constant pressure (J/kgK)
CRF	Capital recovery cost
$C_{\epsilon 2}$	Turbulent equation model constant
C_μ	Turbulent equation model constant
d	Diameter (m)
$\dot{E}$	Energy rate (W)
FAC	Fixed annual cost ($)
h_∞	Heat transfer coefficient between glass and ambient (W/m^2K)
I	Solar radiation (W/m^2)
int	interest rate (%)
k	Thermal conductivity (W/mK)
L	Distance (mm)
$\dot{m}$	Mass flow rate (kg/s)
n	Lifespan (year)
N_{days}	Number of sunny days
$\dot{P}$	Energy consumption rate (W)
P	Pressure (Pa)
P_c	Capital cost ($)
PV	Photovoltaic
PVT	Photovoltaic thermal
r	Radius (mm)
R_x	Exergoeconomic parameter (kWh/$)
SF	Sinking fund factor
T	Temperature (K)
u	Velocity (m/s)
UAC	Uniform annual cost ($)
x	Distance in x direction (mm)
$\dot{X}$	Exergy rate (W)
y	Distance in y direction (mm)

Greek Symbols

α	Absorptivity
β	temperature coefficient 1/°C
η	Efficiency (%)
μ	Dynamic viscosity (Ns/m^2)
ρ	Density (kg/m^3)
σ	Turbulent Prandtl number
τ	Transmissivity

Subscripts

a	Ambient
ab	Absorbed
c	Cell
e	Electrical
en	Energy
e,n	Net electrical
e,x	Entry/exit in x direction
e,y	Entry/exit in y direction
f	Fan
fl	Fluid
g	Glass
i	Inlet
l	Loss
m,i	Mass flow rate for the inlet
m,o	Mass flow rate for the outlet
o	Outlet, Overall
ref	Reference
s	Solid
t	Thermal
w	Wind
x	Exergy

generation of electrical and thermal energy, meeting user demand with a single system while producing more energy per unit area compared to standalone PV modules or solar thermal collectors [14,15]. PVT collectors primarily utilize air and water as cooling fluids [16,17]. Despite poor thermophysical properties of air, its use as a coolant in PVT collectors is advantageous due to the minimal material requirements, leading to cost-effective solutions [18]. Therefore, air-cooled PVT collectors could be unified into building facades and roofs, helping to remove the surplus heat from the PV panel while also meeting ventilation and heating needs of the building [19].

Many studies have been carried out in the literature to boost the thermal and electrical efficiency in air-cooled PVT collectors [20,21]. To enhance the efficiency of the air-cooled PVT collector, Singh et al. [22] conducted an optimization process, considering parameters such as channel length and depth, airflow rate within the channel, the thickness of the Tedlar and glass layers, and the temperature of the incoming fluid. The optimization process significantly enhanced both the electrical and thermal efficiencies of the system. Fan et al. [23] incorporated longitudinal fins into the air duct of a PVT-SAH collector to enhance useful thermal energy and net electrical output. They conducted an optimization study considering construction materials, geometric configurations, and functional parameters. The results revealed that the optimized design significantly outperformed other basic configurations, achieving notable improvements in both thermal and electrical efficiencies. Tahmasbi et al. [24] introduced metal foams in the air channel beneath the PV cells to enhance cooling and improve both thermal and electrical efficiencies. Their study demonstrated that the inclusion of porous media resulted in significant gains in both efficiencies. However, they highlighted that beyond a certain thickness, the metal foams led to a substantial increase in pressure loss, which adversely affected several critical performance factors of the PVT system. Ozakin and Kaya [25] investigated the energy and exergy performance of a PVT system with air cooling. Utilizing ANSYS Fluent, they compared three scenarios: no fins, frequent fins, and sparse fins. Their results indicated that both frequent and sparse fins significantly enhanced the thermal and electrical efficiencies when compared to the no-fin scenario, highlighting the critical role of fin structures in improving the performance of air-cooled PVT collectors. Arslan et al. [26] designed an air-cooled PVT collector and tested it at varying air flow rates. The uniqueness of the design was the increase in the number of holes and the height of the copper fins from the inlet to the outlet of the collector. The electrical, thermal, and environmental performance indicators of the PVT collector were evaluated by varying the airflow rate at different fan voltages. The optimal results were achieved when the fan operated at the highest voltage (12 V), demonstrating the significant impact of voltage on the performance of the system.

Solar air heaters (SAHs) are another solar energy technology that utilizes air as the working fluid, features a simple structural geometry, and offers a highly cost-effective solution for thermal energy production [27]. In recent years, extensive research has focused on the development of roughened surfaces and fin configurations on absorber plates to enhance the thermal performance of SAHs [28–31]. In this context, Patel

[32] conducted a numerical study on the thermal performance and friction factor properties of a SAH, with various artificial fins such as circular wire, rectangle, semicircle, isosceles triangle, combinations of quarter circle-square-triangle, and NACA profiles. The study found that the most optimal performance was achieved with NACA profile fins. The positive impact of NACA profiles in solar air heaters has garnered attention from some researchers, prompting investigations into the effects of various NACA profiles, such as NACA 0020 and NACA 0040, in these systems [33–36]. Patel et al. [34] conducted an optimization of a novel reversed NACA 0040 rib profile to augment the performance of SAH. They optimized some parameters, such as the groove angle and the spacing/width between grooves for different Reynolds numbers (varying between 6000 and 18000). Optimal results identified were a groove angle of 30°, a spacing ratio of 0.167, and a groove width ratio of 1.333. Kumar et al. [35] numerically compared four different rib profiles in SAHs. The profiles included a square rib, a semi-circular rib, a forward-facing symmetric half NACA 0020, and a backward-facing symmetric half NACA 0020. The highest thermo-hydraulic performance values were found for the backward-facing symmetric half NACA 0020 profile. Consequently, NACA 0020 profiles were recommended by researchers for solar air heater applications due to their ability to reduce flow resistance while maintaining high thermal performance.

Recent numerical studies have demonstrated that incorporating NACA airfoils in solar air heaters significantly enhances their performance by simultaneously minimizing pressure drop and enhancing convective heat transfer. Unlike solar air heaters, air-cooled PVT collectors generate both electrical and thermal energy. Improving heat transfer in PV panels directly increases the production of both energy types. However, it is essential to consider pressure drop losses that may accompany these improvements. While different NACA profiles have yielded promising results in solar air heaters, their effects on air-cooled PVT collectors remain unexplored. This represents a critical gap in the literature that warrants further investigation to better understand their potential impact. In this context, the use of a cambered and aerodynamically efficient profile such as NACA 8412, which has not been previously applied in any PVT system, offers a unique opportunity to enhance both thermal and electrical outputs simultaneously.

To address this gap in the literature, this study numerically analyzes the impact of incorporating NACA 8412 model airfoils into air-cooled PVT collectors on their energetic and exergetic performance parameters. Initially, the impact of placing NACA 8412 model airfoils at different distances along the length and width of the PV panel on the performance parameters was explored. This spatial arrangement strategy, in which the airfoils are staggered within the duct in both longitudinal and transverse directions rather than being fixed to the absorber surface, introduces a novel methodological approach. The design analyses conducted in this study have not been found in the existing literature. This represents the first originality in the research. In addition, economic and environmental analyses were also conducted as part of the study. Finally, using the numerical data sets obtained within the scope of the study, different Artificial Neural Network (ANN) models were created to estimate important output parameters for the PVT collector employing NACA 8412 model airfoils, and the best performing models were identified. The most noteworthy feature of the ANN models is that they encompass many design and operational parameters. Thus, very comprehensive ANN models have been developed—both for single and multi-output estimations—which constitutes the secondary originality of the study and extends its practical applicability.

2. Methodology

This study encompasses the numerical modeling of NACA 8412 airfoils, their integration into the PVT collector, the performance evaluation based on energy, exergy, economic, and environmental analyses, and the prediction of key outputs using artificial neural networks. This methodological process is presented in the flowchart in Fig. 1.

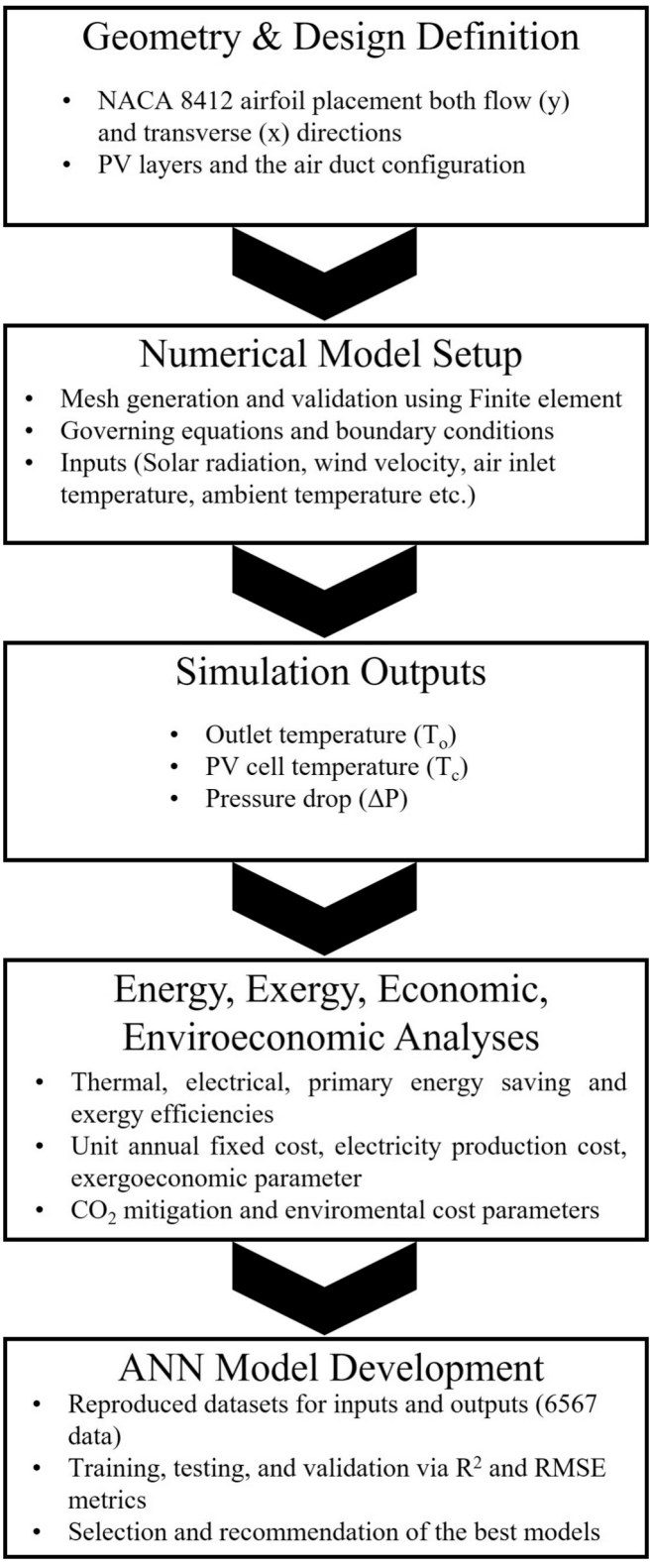

Fig. 1. Flowchart of the methodological steps.

2.1. Model geometry and key design parameters

The PVT collector is composed of the layers illustrated in Fig. 2-**a**, and numerical analyses were conducted based on this layering sequence (Fig. 2-**a** and **2-b**). Table 1 depicts the dimensions for the various elements of the PVT collector. Table 2 provides the materials used in the

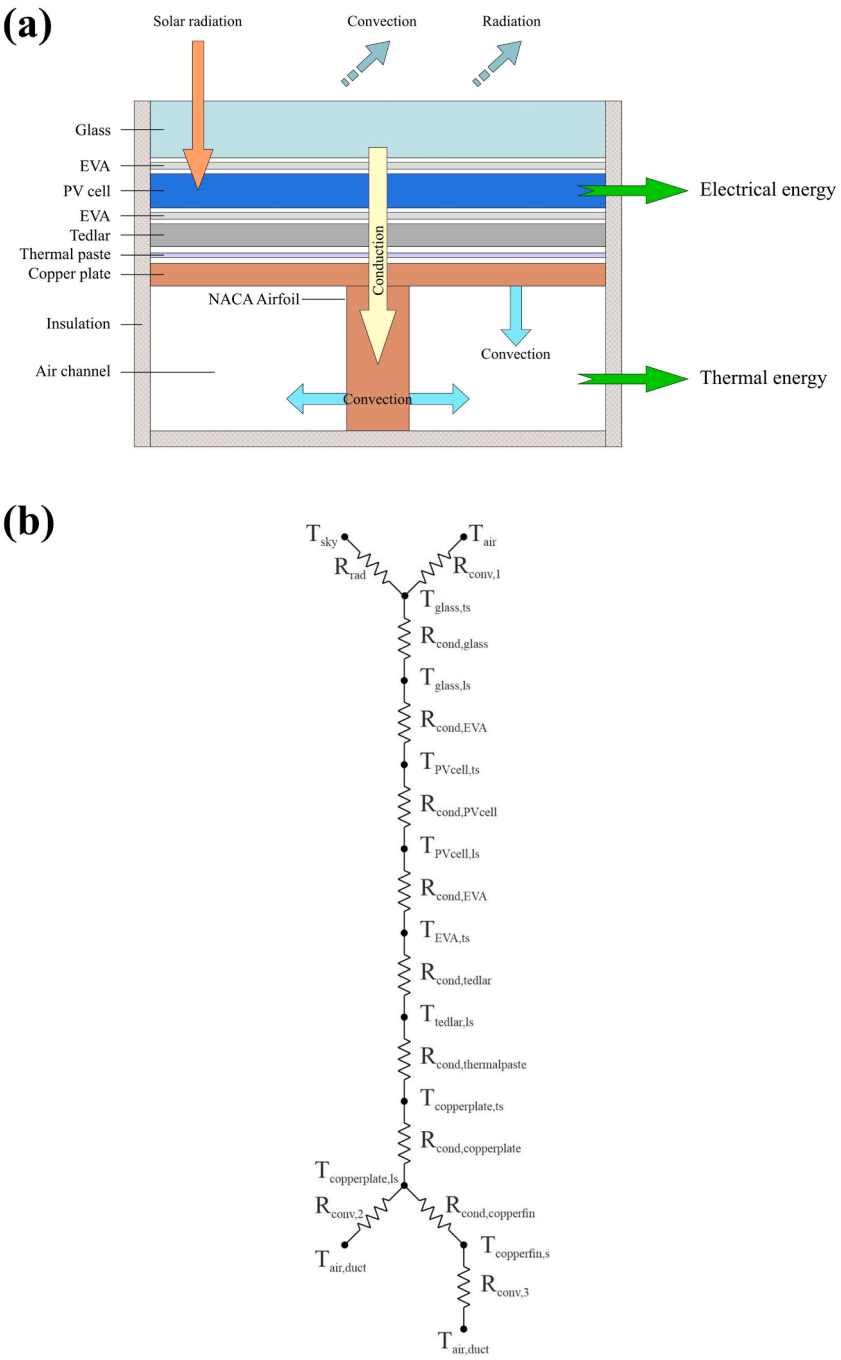

Fig. 2. Schematic representation of structure, energy balance phenomena (a) and thermal network diagram for PVT (b).

Table 1
The sizes of each element for the PVT.

Element	Sizes (mm)
Glass	680 × 370 × 3.0
EVA	680 × 370 × 0.5
PV cell	680 × 370 × 0.3
Tedlar	680 × 370 × 0.1
Thermal paste	680 × 370 × 0.3
Copper absorber	680 × 370 × 0.4
Air duct	680 × 370 × 10

Table 2
The materials and their thermophysical properties in the PVT.

Material	c_p (J/kgK)	ρ (kg/m^3)	k (W/mK)
Glass	500	2500	1.8
EVA	2090	960	0.35
PV cell	700	2330	148
Tedlar	1250	1200	0.20
Thermal paste	700	2600	1.9
Copper absorber/airfoils	385	8960	401

PVT collector along with their thermophysical characteristics. In this study, the NACA 8412 model airfoil was used for the purpose of cooling the PV panel (Fig. 3-**a**). The placements of the airfoils at different

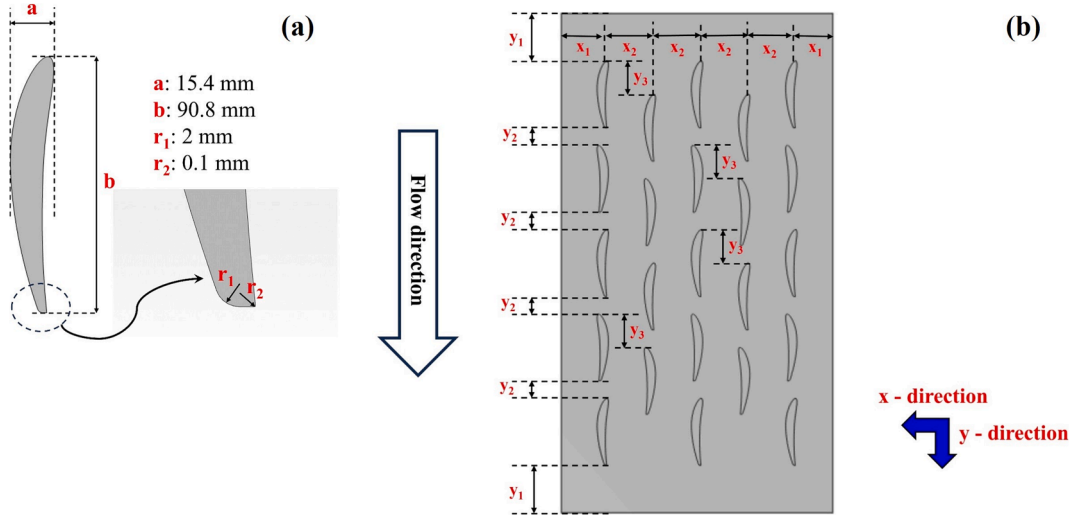

Fig. 3. Geometry and dimensions of NACA 8412 model airfoils (a) and a view of the arrangement of the NACA 8412 model airfoils in the PVT collector (b).

distances were numerically examined, and the electrical and thermal effects of the PVT collector were investigated. Fillet was added to sharp corners of airfoils to better quality mesh (r_1 and r_2). The total length of the airfoil is 90.8 mm (length b), the total width of the airfoil is 15.4 mm (length a) and depth of the airfoil is 10 mm. The depth of the airfoil and the depth of the air channel of PVT collector are the same. The NACA 8412 model airfoils are staggered with respect to the PV panel (Fig. 3-**b**). The direction from the inlet to the outlet of the air channel of the PVT collector (the flow direction) is referred to as the y-direction. y_1 is the distance of the airfoil profiles from the inlet and outlet mouths of the PVT collector in the y-direction. The y_1 distance is referred to as $L_{e,y}$, which was modified from 5 mm to 105 mm in numerical analysis. The spacing between the airfoil profiles in the y-direction is uniformly distributed and denoted as y_2. The perpendicular to the flow direction of the PVT collector is referred to as the x-direction. x_1 is the distance of the airfoils from the far right and left edges of the panel inward in the PVT collector. The x_1 distance is referred to as $L_{e,x}$ and was varied at intervals of 5 mm from 5 mm to 65 mm in numerical analysis. The spacing between the airfoil profiles in the x-direction is uniformly distributed and denoted as x_2. There is a distance of 45.38 mm between the airfoils arranged in the 1st, 3rd, and 5th rows and the 2nd and 4th rows along the x-axis, and this distance is called y_3.

2.2. Numerical procedure

In this study, numerical analyses were performed using the COMSOL Multiphysics software. The following simplifying assumptions were made:

- The Multiphysics interface was configured to use non-isothermal flows.
- It was assumed that the EVA layer is fully transparent with 100 % transmission efficiency, which is a common simplification frequently adopted in the literature for modeling purposes [37,38].
- It was assumed that all components of the PVT collector are in perfect contact with each other.
- The collector inlet air temperature was considered to be equal to the ambient temperature.
- The temperature variation caused the air flow temperature to vary. The library in COMSOL Multiphysics was utilized for this process.
- Dust effects on the glass layer's upper surface were neglected.

The heat conduction equation was used to calculate heat transfer from the top surface of the PVT to the surfaces of the fins and the copper plate. For the airflow in the collector, a combined heat transfer solution was applied, as the heat transfer between the surfaces of the copper plate and fins and the flowing fluid included both conduction and convection. **Eqs. (1) and (2)** denote the energy conservation and Fourier heat conduction solution, respectively [39].

$$\left(\rho c_p u_j \nabla T_j\right) + \nabla q = Q \tag{1}$$

$$-k_{fl}\nabla T_j = q \tag{2}$$

The mass and momentum conservations are described by **Eqs. (3) and (4)**, considering the incompressible and Newtonian properties of the coolant fluid [39].

$$\rho \bullet \nabla u_j = 0 \tag{3}$$

$$(\rho\cdot\nabla)\cdot u_j = \nabla\cdot[-PI + (\mu+\mu_T)\cdot(\nabla u_j + \left((\nabla u_j)^T\right) + F + p\cdot g \tag{4}$$

The flow regime is turbulent, and the flow of the fluid is assumed to be incompressible, uniform, and steady-state. The Realizable k-ε model was chosen for numerical solutions to address the turbulent flow. **Eqs. (5) and (6)** were utilized to calculate the turbulence kinetic energy (k) and the energy dissipation rate (∈) [40,41].

$$\nabla(\rho k u_j) = \nabla\left[\left(\mu\frac{\mu_T}{\sigma_k}\right)\nabla k\right] + G_k - \rho\epsilon \tag{5}$$

$$\nabla(\rho\epsilon u_j) = \nabla\left[\left(\mu\frac{\mu_T}{\sigma_\epsilon}\right)\nabla\epsilon\right] - \rho C_{\epsilon 2}\frac{\epsilon^2}{k+\sqrt{\nu\epsilon}} \tag{6}$$

where, σ_k=1 and σ_ϵ = 1.2. G_k depicts the production of turbulent kinetic energy and is determined using the following equations:

$$G_k = \mu_T S^2 \tag{7}$$

$$\eta = S\frac{k}{\epsilon} \tag{8}$$

$$S = \sqrt{2S_{ij}S_{ij}} \tag{9}$$

$$\mu_t = \rho C_\mu \frac{k^2}{\varepsilon} \tag{10}$$

$$C_\mu = \frac{1}{A_0 + A_s U^* \frac{k}{\in}} \tag{11}$$

where, $A_0 = 4$ and $A_s = \sqrt{6}cos\phi$. The model constants are determined as follows:

$$\begin{aligned} \phi &= \frac{1}{3} cos\phi^{-1}\left(\sqrt{6}\, W\right), \\ W &= \frac{2\sqrt{2} S_{ij} S_{jk} S_{ki}}{\widetilde{S}^3}, \\ \widetilde{S} &= \sqrt{S_{ij} S_{ij}}, \\ S_{ij} &= \frac{1}{2}\left(\frac{\partial u_j}{\partial x_i} + \frac{\partial u_i}{\partial x_j}\right) \end{aligned} \tag{12}$$

U* can be estimated using the following equations:

$$U^* = S_{ij} S_{ij} + \widetilde{\Omega}_{ij} \widetilde{\Omega}_{ij} \tag{13}$$

$$\widetilde{\Omega}_{ij} = \Omega_{ij} - 2\epsilon_{ijk}\omega_k \tag{14}$$

$$\Omega_{ij} = \overline{\Omega}_{ij} - \epsilon_{ijk}\omega_k \tag{15}$$

where, $\overline{\Omega}_{ij}$ is the mean rate-of-rotation tensor dependent on the angular velocity (ω_k).

The boundary conditions applied in the numerical analyses are as follows [37,38]:

- Solar radiation was applied to the upper surface of the PV panel, where both convective and radiative heat losses were considered.:

$$-n \bullet q = h_\infty \bullet \left(T_a - T_g\right) \tag{16}$$

$$-n \bullet q = \varepsilon \bullet \sigma \bullet \left(T_{sky} - T_g\right) \tag{17}$$

- With the PVT collector, it was assumed that the bottom and side surfaces were fully insulated:

$$-n \bullet q = 0 \text{ (adiabatic)} \tag{18}$$

- The no-slip condition was applied to solid walls:

$$u = 0 \tag{19}$$

- A uniform flow velocity and inlet fluid temperature are imposed at the entrance of the channel.

$$v = v_i \tag{20}$$

$$T = T_i \tag{21}$$

- The outlet pressure of the air duct was considered to be 0

$$P_o = 0 \tag{22}$$

- The boundary condition for the solid–fluid interface was defined as

$$\left(\frac{\delta T_s}{\delta n}\right)_{fl} = \frac{k_s}{k_{fl}} \left(\frac{\delta T_s}{\delta n}\right)_s \tag{23}$$

2.3. Energy analysis

Using energy balance equations, thermal and electrical energy generated by the PVT collector can be obtained. The energy balance for the control volume under steady-state conditions is expressed as **Eq. (24)** [42].

$$\dot{E}_{ab} = \dot{E}_e + \dot{E}_t + \dot{E}_l \tag{24}$$

$\dot{E}_{ab}$, $\dot{E}_e$, $\dot{E}_t$, and $\dot{E}_l$ represent the absorbed solar radiation energy rate, the electrical energy production rate, the thermal energy production rate, the thermal losses, respectively. Absorbed solar radiation is calculated by **Eq. (25)**. In the analyses, τ and α was assumed to be 0.92 and 0.9, respectively [43].

$$\dot{E}_{ab} = I \bullet \tau \bullet \alpha \bullet A_{PV} \tag{25}$$

The rate of thermal energy production is determined by the air mass flow rate ($\dot{m}_{air}$), the specific heat capacity of air ($c_{p,air}$), and the temperature difference between the air entering and exiting the PVT collector. This relationship is expressed in **Eq. (26)** [42].

$$\dot{E}_t = \dot{m}_{air} \bullet c_{p,air} \bullet \left(T_o - T_i\right) \tag{26}$$

The mechanical energy consumption required to overcome friction ($\dot{P}_m$) is calculated by **Eq. (27)** [44].

$$\dot{P}_m = \frac{\dot{m}_{air}}{\rho} \bullet \Delta P \tag{27}$$

where ΔP is the pressure drop that occurs in the air entering and leaving the collector.

Heat transfer coefficient (h_∞) from the top of the glass to the ambient air is a function of wind velocity (v_w) and is expressed by **Eq. (28)** [45].

$$h_\infty = 5.7 + 3.8 \bullet v_w \tag{28}$$

The thermal efficiency (η_t) is calculated using **Eq. (29)** [46].

$$\eta_t = \frac{\dot{E}_t}{\dot{E}_{ab}} \tag{29}$$

The net electrical energy production rate is calculated as the difference between the electrical energy production rate ($\dot{E}_e$) and the energy consumption rate by the fan ($\dot{E}_f$) [47,48].

$$\dot{E}_{e,n} = \dot{E}_{ab} \bullet \left(\eta_{ref} \bullet \left[1 - \beta\left(T_c - T_{ref}\right)\right]\right) - \dot{E}_f \tag{30}$$

$$\dot{E}_f = \frac{\dot{P}_m}{\eta_f} \tag{31}$$

where, η_f represents the efficiency of the fan and is assumed to be 0.65 in this study [49]. β is assumed to be 0.0045 1/°C at the reference temperature (T_{ref} = 25 °C) in the analysis.

The electrical efficiency (η_e) is calculated using **Eq. (32)** [47].

$$\eta_e = \frac{\dot{E}_{e,n}}{\dot{E}_{ab}} \tag{32}$$

While overall PVT efficiency is often calculated as the sum of thermal and electrical efficiencies, this approach overlooks the higher-grade

nature of electrical energy. To address this, primary energy-saving efficiency (η_{PES}) is used, enabling a more accurate comparison based on the first law of thermodynamics [50]. The electrical output is converted to its thermal equivalent using a coefficient of 0.38, reflecting the typical efficiency of conventional power plants. The η_{PES} is calculated using **Eq. (33)** [50].

$$\eta_{PES} = \eta_t + \frac{\eta_e}{0.38} \tag{33}$$

2.4. Exergy analysis

Exergy represents the maximum achievable work that a mass or energy flow can deliver when brought into equilibrium with a defined reference state [51]. The exergy analysis of a PVT collector encompasses several parameters, including the exergy input from solar radiation, output exergies (thermal and electrical), and exergy losses. The overall exergy balance for the system is typically represented by **Eq. (34)** [50].

$$\dot{X}_i = \dot{X}_o - \dot{X}_l \tag{34}$$

$$\dot{X}_i = \dot{E}_{ab}\left[1 - \frac{4}{3}\left(\frac{T_i}{T_{sun}}\right) + \frac{1}{3}\left(\frac{T_i}{T_{sun}}\right)^4\right] \tag{35}$$

$$\dot{X}_o = \dot{X}_t + \dot{X}_{e,n} \tag{36}$$

In this analysis, the inlet temperature and the outdoor temperature are assumed to be equal. T_{sun} is considered to be 5777 K, representing the temperature of the sun. The net electrical exergy ($\dot{X}_{e,n}$) and thermal exergy ($\dot{X}_t$) were determined using **Eqs. (37) and (38)**, respectively [38].

$$\dot{X}_{e,n} = \dot{E}_{e,n} \tag{37}$$

$$\dot{X}_t = \dot{E}_t \bullet \left(1 - \frac{T_i + 273.15}{T_o + 273.15}\right) \tag{38}$$

The exergy efficiency is evaluated using **Eq. (39)** [38].

$$\eta_x = \frac{\dot{X}_o}{\dot{X}_i} = 1 - \frac{\dot{X}_l}{\dot{X}_i} \tag{39}$$

2.5. Economic analysis

To conduct the economic analysis of the present PVT collector, the initial step involves determining the uniform annual cost (UAC). This cost accounts for three primary components: the fixed annual cost (FAC), the annual maintenance cost (AMC), and the annual salvage value (ASV). The UAC is evaluated using **Eq. (40)** [52,53].

$$UAC = FAC + AMC - ASV \tag{40}$$

The FAC represents the fundamental expenditure necessary for system operation and is determined using **Eq. (41)** [52,53].

$$FAC = CRF \bullet P_c \tag{41}$$

The parameter P_c denotes the capital of key PVT components (PV panel, copper plate and fins, fan, insulation, etc.), with prices adopted from literature values [54,55]. The capital recovery factor (CRF), used to annualize this capital cost, is computed using **Eq. (42)** [52,53].

$$CRF = \frac{int(1+int)^n}{(1+int)^n - 1} \tag{42}$$

In this context, n and int represent the lifespan of the system and the annual interest rate, respectively. The AMC is typically assumed to be 10 % of the FAC [52,53].

The ASV of the PVT collector is determined by multiplying the salvage value (S) by the sinking fund factor (SF), as expressed in **Eq. (43)** [52,53].

$$ASV = S \bullet SF \tag{43}$$

$$SF = \frac{int}{(1+int)^n - 1} \tag{44}$$

Net electricity production cost ($C_{e,n}$) is calculated using **Eq. (45)** [52,53].

$$C_{e,n} = \frac{UAC}{E_{e,n-yearly}} \tag{45}$$

where $E_{e,n\text{-yearly}}$ is the annual net electrical energy obtained from the PVT collector. The annual net electrical energy gain was calculated by summing daily hourly values, scaling by the number of clear days per month, and then aggregating monthly totals.

The exergoeconomic approach is a methodology that integrates exergy analysis with economic principles to evaluate and enhance the performance of energy systems. [53]. Given that exergy captures the significance of thermodynamic effects, cost allocation based on exergy provides a meaningful basis for analysis in energy conversion technologies. A higher exergoeconomic parameter (R_x) indicates greater exergy gain and reduced product cost, both of which are desirable characteristics in PV technologies. This parameter can be calculated using **Eq. (46)** [52].

$$R_x = \frac{UAC}{X_{o-yearly}} \tag{46}$$

where $X_{o\text{-yearly}}$ is the annual exergy output obtained from the PVT collector. The annual exergy output was obtained by summing daily hourly values, multiplying by monthly clear days, and totaling the monthly outputs. Economic analyses were performed for provinces with different climatic conditions—Mersin (Me), Muğla (Mu), and Trabzon (Tr)—taking into account their number of sunny days [56,65].

2.6. Enviroeconomic analysis

Electricity generation from clean energy sources offers significant potential for mitigating harmful greenhouse gas (GHG) emissions [52,57]. Among these, carbon dioxide (CO_2) is particularly detrimental to both human health and environmental quality [38,58]. In this context, environmental analyses were conducted to assess the carbon emission reduction potential of the air-cooled PVT collector equipped with NACA airfoils as a sustainable alternative to conventional fossil fuel-based systems. The annual CO_2 mitigation parameters, based on both energy ($\varnothing_{CO_2,en}$) and exergy ($\varnothing_{CO_2,x}$) approaches, are quantified using **Eqs. (47) and (48)**, respectively [53].

$$\varnothing_{CO_2,en} = \frac{\Psi_{CO_2} \bullet \dot{E}_{en} \bullet N_{days}}{1000} \tag{47}$$

$$\varnothing_{CO_2,x} = \frac{\Psi_{CO_2} \bullet \dot{E}_{x} \bullet N_{days}}{1000} \tag{48}$$

In these equations, $\dot{E}_{en}$ and $\dot{E}_x$ represent the annual energy and exergy outputs, respectively. The parameter Ψ_{CO_2} denotes the average carbon dioxide emission factor for coal-based electricity generation and is assumed to be 2.08 kg CO_2/kWh. N_{days} denotes the number of sunny days in a year considered in the analysis; in this study, three provinces

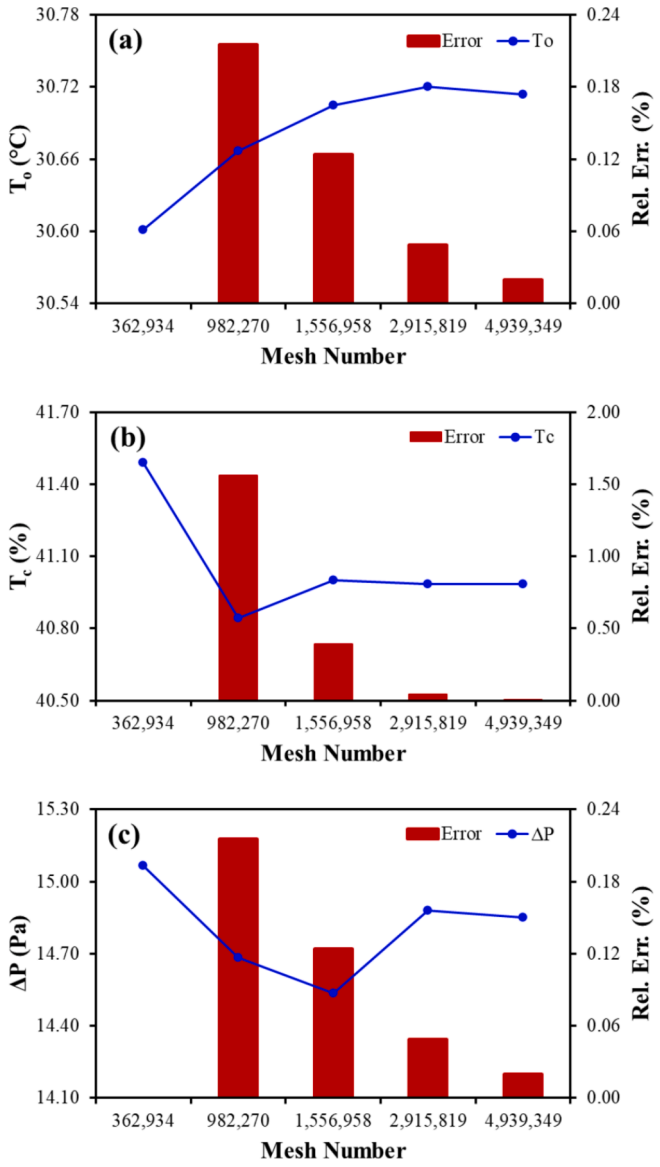

Fig. 4. Grid independency test and the relative errors.

with different climatic conditions [65]—Me, Mu, and Tr—were taken into account for the number of sunny days [56].

The annual environmental cost parameters, based on energy ($Z_{CO_2,en}$) and exergy ($Z_{CO_2,x}$), are evaluated using **Eqs. (49) and (50)**, respectively [53].

$$Z_{CO_2,en} = P_{CO_2} \bullet \varnothing_{CO_2,en} \tag{49}$$

$$Z_{CO_2,x} = P_{CO_2} \bullet \varnothing_{CO_2,x} \tag{50}$$

where, P_{CO_2} represents the carbon price per ton of CO_2, which is taken as an average value of 14.5 \$/tCO_2 in this study.

2.7. Mesh generation and grid independence test

A grid independence trial was conducted for revealing the reliability of the numerical solution. In the discretization process, a free tetrahedral mesh generation was performed in the fluid, copper fins, and the lower surface area of the copper plate, while a free triangular mesh production was used for the other boundary elements. Additionally, a boundary layer mesh was introduced on the fluid side between the solid surface and the fluid to account for boundary layer effects. Inlet velocity of the fluid is 3.5 m/s. For the test, the solar radiation was set to 1000 W/m^2, and the inlet and outdoor air temperatures were fixed at 25 °C. The parameters considered were the outlet air temperature (T_o), cell surface temperature (T_c), and pressure difference between the collector inlet and outlet air (ΔP). The number of elements adopted in the mesh area for the base model ranged from 362,934 to 4,939,349, and the calculated outlet air temperature, cell temperature, and pressure drop were compared with each other to define grid independence criteria. The grid independence test results are displayed in Fig. 4, where the relative

Table 3
Properties the ANN models that were created.

First Group	Model number	Neuron in Layers
	1	8–5-1
	2	8–10-1
	3	8–15-1
	4	8–20-1

Second Group	Model number	Neuron in Layers
	1	8–5-3
	2	8–10-3
	3	8–15-3
	4	8–20-3

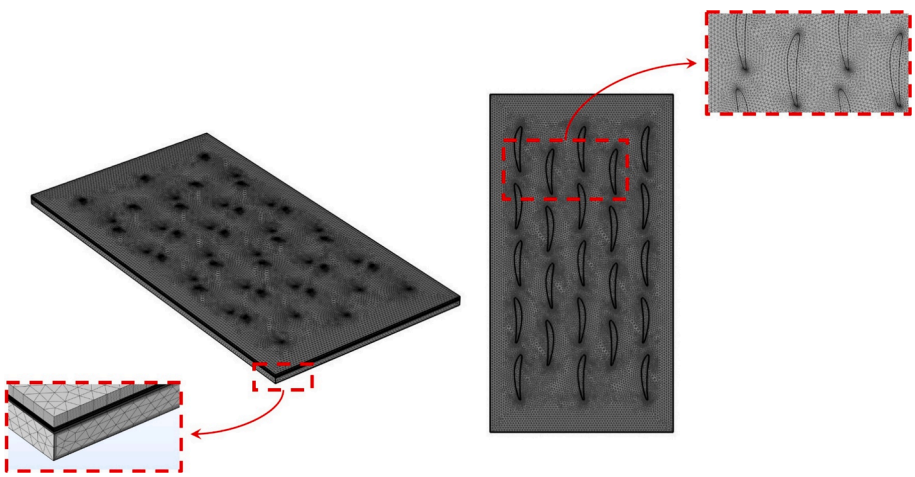

Fig. 5. The depiction of the chosen grid arrangement for the PVT collector.

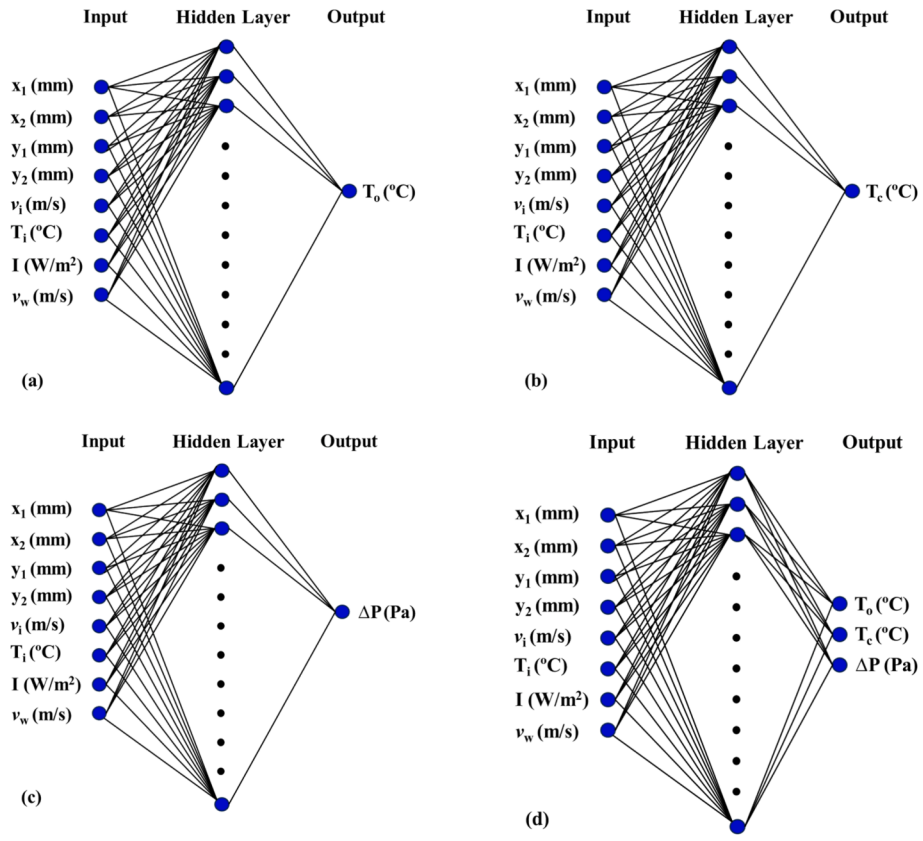

Fig. 6. Structure of generated ANN models for estimating one output parameter (a – c) and all output parameters (d).

Table 4
Ranges of input parameters used in the development of ANN models.

Input parameter	Unit	Range
x_1	mm	0–65
x_2	mm	0–70.80
y_1	mm	0–105
y_2	mm	0–56.06
v_i	m/s	2–6
T_i	°C	25–40
I	W/m^2	200–1000
v_w	m/s	0–4

errors for the number of elements 2,915,819 and 4,939,349 were calculated as 0.02 % for outlet air temperature, 0.0003 % for cell temperature, and 0.18 % for pressure drop. It was concluded that the relative error for the number of elements between 2,915,819 and 4,939,349 was less than 0.5 % for the parameters considered, indicating that working with the mesh count in this range could be confidently done. Therefore, all numerical analyses were performed using a mesh structure with 3,286,478 elements (Fig. 5).

2.8. Artificial neural networks (ANNs) modeling

Different ANN models with various structures were created for the key output parameters of the air-cooled PVT collector with NACA 8412 airfoils, and the most suitable models were determined for usage. The output parameters for ANN models include collector outlet air temperature (T_o), cell temperature of PV panel (T_c), and pressure difference between inlet and outlet air (ΔP). The input parameters selected are geometric and operational parameters that affect the performance of the air-cooled PVT collector using NACA 8412 airfoils. The geometric input parameters are the distances from the edges of the panel to the inside for

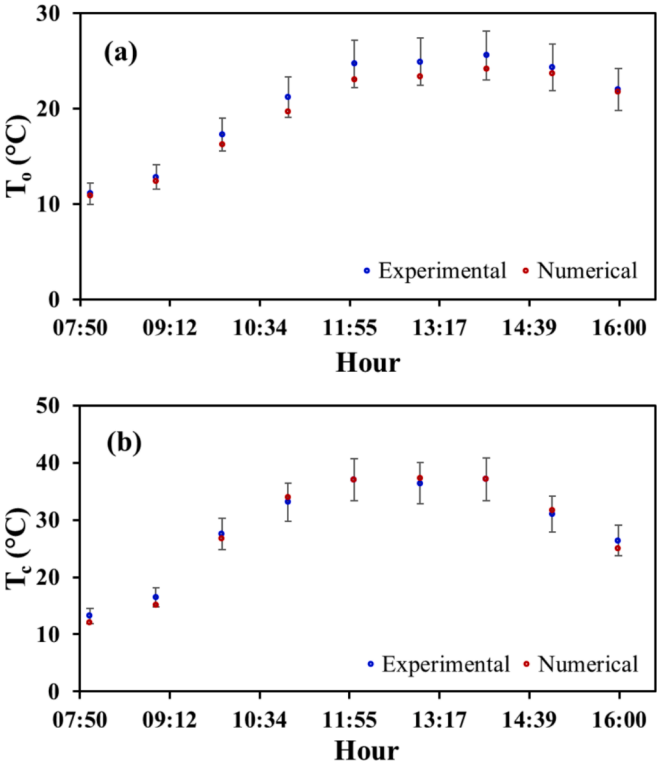

Fig. 7. Comparison results obtained from current study and experimental data reported by Tiwari et al. [59].

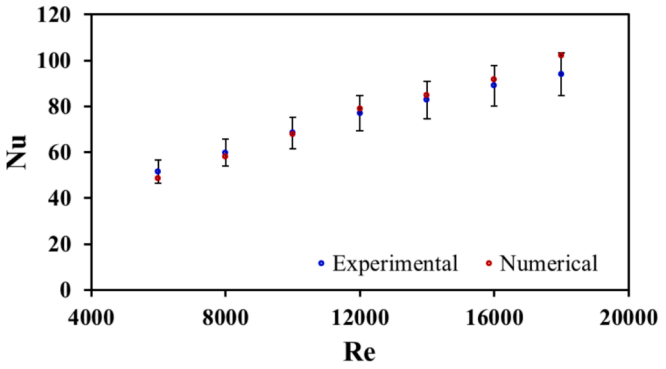

Fig. 8. Comparison results obtained from current study and experimental data for NACA 0040 profile rib reported by Patel et al. [33].

Table 5
Input parameters used in numerical analysis.

Parameter	Unit	Base-case	Variable
v_i	m/s	–	2–6
I	W/m^2	1000	–
v_w	m/s	2	–
T_i	°C	25	–

the rightmost and leftmost positioned airfoils (x_1), the distance between the airfoils in the x-direction of the PV panel (x_2), the distances from the inlet and outlet mouths of the airfoils in the y-direction (the flow direction) (y_1), and the distance between the airfoils in the y-direction (y_2). Cases where x_1, x_2, y_1, and y_2 distances are zero represent a flat plate PVT collector. To ensure that the ANN models could encompass a broad range of geometries and operating conditions in the designed air-cooled PVT collector, extensive numerical simulations were performed across diverse operating parameters, resulting in the generation of a comprehensive dataset. The operational input parameters are the inlet air velocity (v_i), inlet air temperature (T_i), irradiation (I), and wind speed (v_w). In the study, the developed ANN models were classified into two groups (Table 3). The first group involves separate ANN models for each output parameter individually (from Fig. 6-**a** to **c**). The second group involves a single ANN model for all output parameters considered (Fig. 6-**d**). The total number of inputs used in developing ANN models is 4776, and the number of outputs is 597 for first group and 1791 for second group, respectively. 60 % of this data was used for training, 20 % for validation, and the remaining 20 % for testing purposes. The generated ANN models used a single hidden layer, testing varying numbers of neurons in the hidden layer (Table 3). The Levenberg-Marquardt Backpropagation algorithm and the Feed Forward Back-propagation algorithm were used as the training function and the training algorithm, respectively. The log-sigmoid (Logsig) transfer function and the linear (Purelin) transfer function were used in the hidden layer and output layer, respectively. Table 4 presents the ranges of input parameters for the ANN models.

2.9. Model validation

In this study, the outputs of the experimental research conducted by Tiwari et al. [59] were used for validation purposes. The PV panel area (0.61 m^2) and the dimensions of the air channel (1.2 x 0.45 x 0.1 m) were adjusted to be the same as those in the experimental setup. An electrical efficiency of 12 % was assumed. For validation, two crucial performance parameters were considered: PV cell temperature (T_c) and collector outlet air temperature (T_o). Fig. 7 demonstrates the trends between experimental and numerical results. It was indicated that all data were within a 10 % relative error margin. For cell temperature, the average and maximum relative errors were found as 3.69 % and 8.97 %, respectively, while for outlet air temperature, the average and maximum relative errors were found as 4.58 % and 7.07 %, respectively.

In this study, a second validation was also performed, focusing on the numerical modeling of the NACA airfoils. Since no experimental study exists for air-cooled PVT collectors with NACA airfoils, validation was based on the experimental data of the Nusselt Number (Nu), a dimensionless heat transfer coefficient representing the ratio of convective to conductive heat transfer at a surface, as reported by Patel et al. [33] for a solar air heater roughened with a NACA 0040 profile rib (C10 plate). The experimental setup included a 1000 mm test section, preceded and followed by 525 mm and 875 mm entrance and exit lengths, respectively. The C10 ribs, with a chord length of 10 mm and a height of 2 mm, were continuously arranged along the absorber plate. The numerical model showed strong agreement with the experimental data across Reynolds numbers (Re) from 6000 to 18000, with a minimum, maximum, and average relative error of 0.83 %, 8.66 %, and 3.73 %, respectively, and all data points falling within a 10 % relative error margin (Fig. 8).

Minor deviations observed in both validation studies are primarily attributed to uncertainties in the experimental boundary conditions and the idealized assumptions adopted in the numerical modeling. Despite these minor discrepancies, the consistent trends and acceptable relative errors demonstrate that the numerical and experimental results are in good agreement.

3. Results and discussion

This study presents a comprehensive numerical investigation of the effects of vertical and horizontal arrangements of NACA 8412 airfoil profiles on the performance of air-cooled PVT collectors. The finite element method was employed for numerical analysis, with all simulations conducted under baseline conditions outlined in Table 5. Initially, the impact of varying NACA 8412 airfoil arrangements along the y-axis on the energetic and exergetic performance parameters of the PVT collector was analyzed. Subsequently, the influence of different airfoil arrangements along the x-axis was examined. Finally, various artificial neural network (ANN) models were developed to predict key output parameters of the PVT collector based on the generated numerical data, and the most accurate models were identified and presented.

3.1. Comparison of NACA 8412 airfoil placement at varying distances in the y-direction ($L_{e,y}$)

Firstly, the effects of NACA 8412 model airfoils placed at different distances in the y-direction on the important metrics of the PVT collector were examined. Since the study primarily examined the impact of different placements of the airfoils in the y-direction, the intervals between all airfoils along the panel in the x-direction were set to be equal ($x_1 = x_2 = 48.86$ mm).

Fig. 9 illustrates the variations in the cell temperature of the PV panel, the outlet air temperature from the PVT collector, and the pressure drop between the inlet and outlet of the collector for different air inlet velocities based on the placement of NACA 8412 model airfoils at different $L_{e,y}$. Across all inlet air velocities, using NACA 8412 model airfoils resulted in lower cell temperature and higher outlet air temperature compared to a flat plate PVT collector. In NACA airfoil-integrated PVT systems, increasing the air velocity from 2 m/s to 5 m/s resulted in a decrease in the air outlet temperature from 35.37 °C to

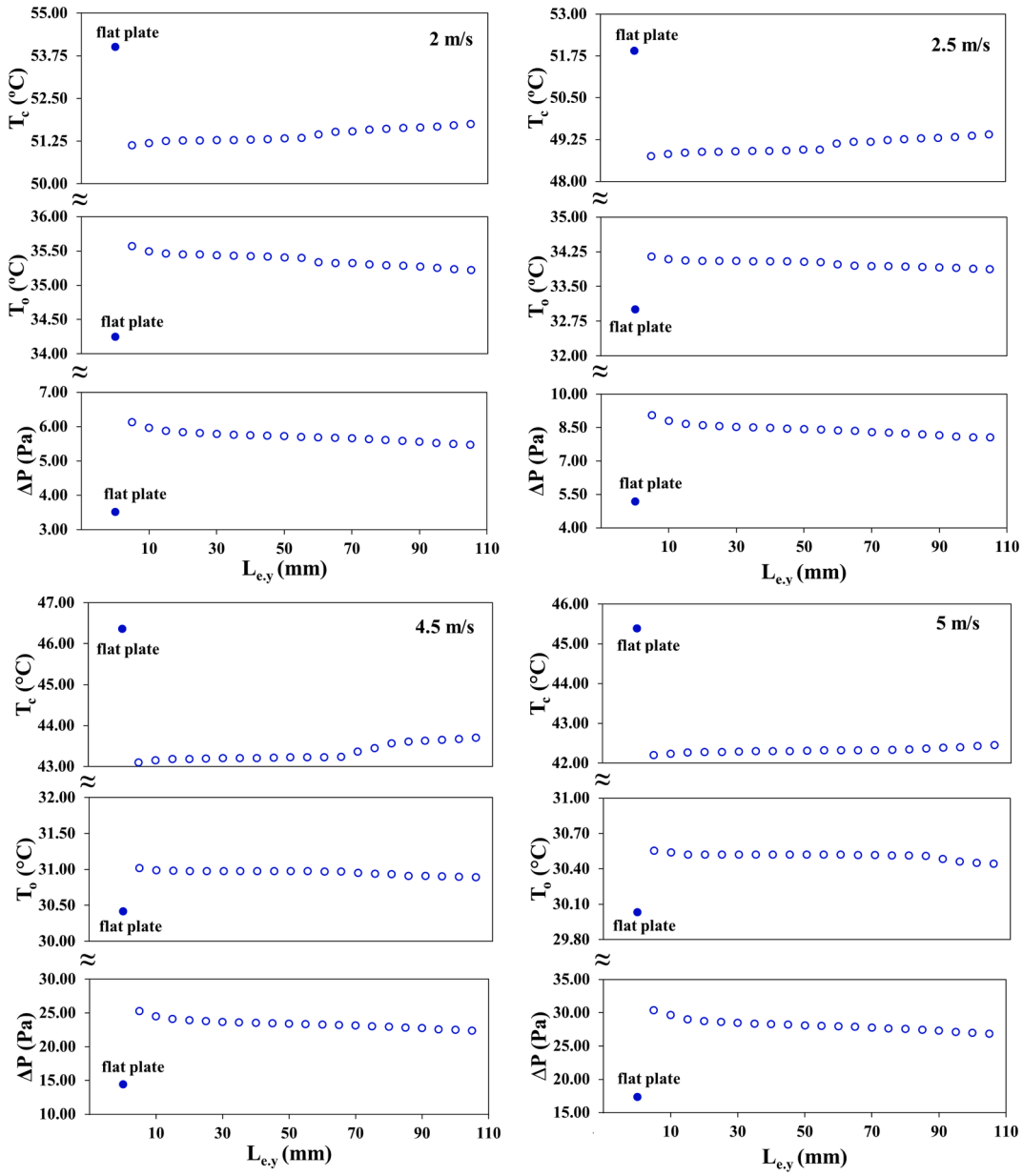

Fig. 9. Variations of T_o, T_c, and ΔP for different $L_{e,y}$ within an inlet velocity range of 2 to 5 m/s.

30.51 °C and in the cell temperature from 51.44 °C to 42.32 °C. Compared to the flat plate collector, this configuration increased the air outlet temperature by 3.26 % and 1.60 %, while reducing the cell temperature by 4.80 % and 6.78 %, respectively. With NACA airfoils, the pressure drop increased from 5.71 Pa to 28.1 Pa as the air velocity rose from 2 m/s to 5 m/s, corresponding to increases of 62.38 % and 61.67 % compared to the flat plate collector. This increasing pressure drop trend can be attributed to the fundamental fluid dynamics within the channel. As the inlet air velocity increases, the Reynolds number rises, leading to a transition to more turbulent flow. When the airflow passes over the NACA 8412 airfoils, it is redirected and disturbed, forming localized vortices and enhancing fluid mixing. These phenomena intensify the wall shear stress and frictional resistance, causing higher pressure losses. At the same time, the elevated turbulence improves convective heat transfer by disrupting the thermal boundary layer and increasing the rate of heat removal from the PV cell and absorber surface. Thus, while higher inlet velocity and the presence of aerodynamic airfoils lead to increased pressure drop, they also contribute to improved heat transfer performance. This highlights the need to balance thermal gains with the associated fan power requirements. The temperature variation indicates that the use of airfoils improves heat transfer compared to a flat plate. However, it was found that the use of airfoils resulted in greater pressure drop compared the flat plate. Second noteworthy result is that as $L_{e,y}$ vary from 5 mm to 105 mm, cell temperature increases gradually, while outlet air temperature and pressure drop decrease progressively. Fig. 10 present the velocity, pressure, and temperature distributions of the air in the PVT collector for $L_{e,y} = 5$ mm, 65 mm, and 105 mm. As $L_{e,y}$ changes from 5 mm to 105 mm, the decrease in velocity reduces the pressure drop within the channel. This occurs because the airfoils are placed farther from the inlet and outlet, resulting in less flow disturbance. The reduced turbulence not only decreases frictional losses, hence pressure drop, but also weakens convective heat transfer by thickening the thermal boundary layer. This explains why heat transfer deteriorates and outlet air temperature shows a decreasing trend, while cell temperature increases with larger $L_{e,y}$ values. In other words, as the $L_{e,y}$ change from 5 mm to 105 mm, the heat transfer deteriorates while the pressure drop improves. The arrangements in the y-direction, which exhibited lower cell temperature and pressure drop

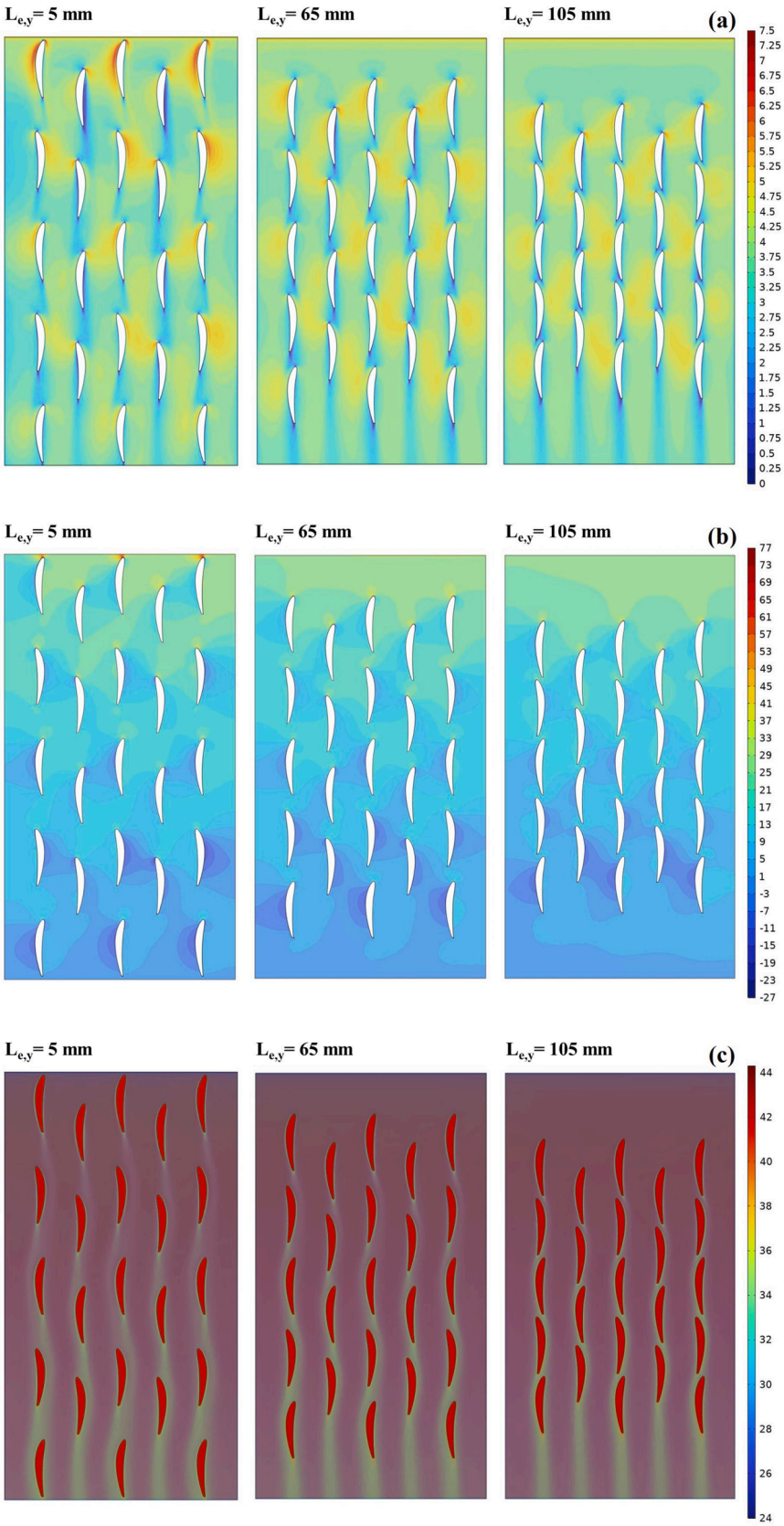

Fig. 10. Velocity (a), pressure (b) and temperature (c) distributions of PVT collectors for different $L_{e,y}$ at $v_i = 5$ m/s.

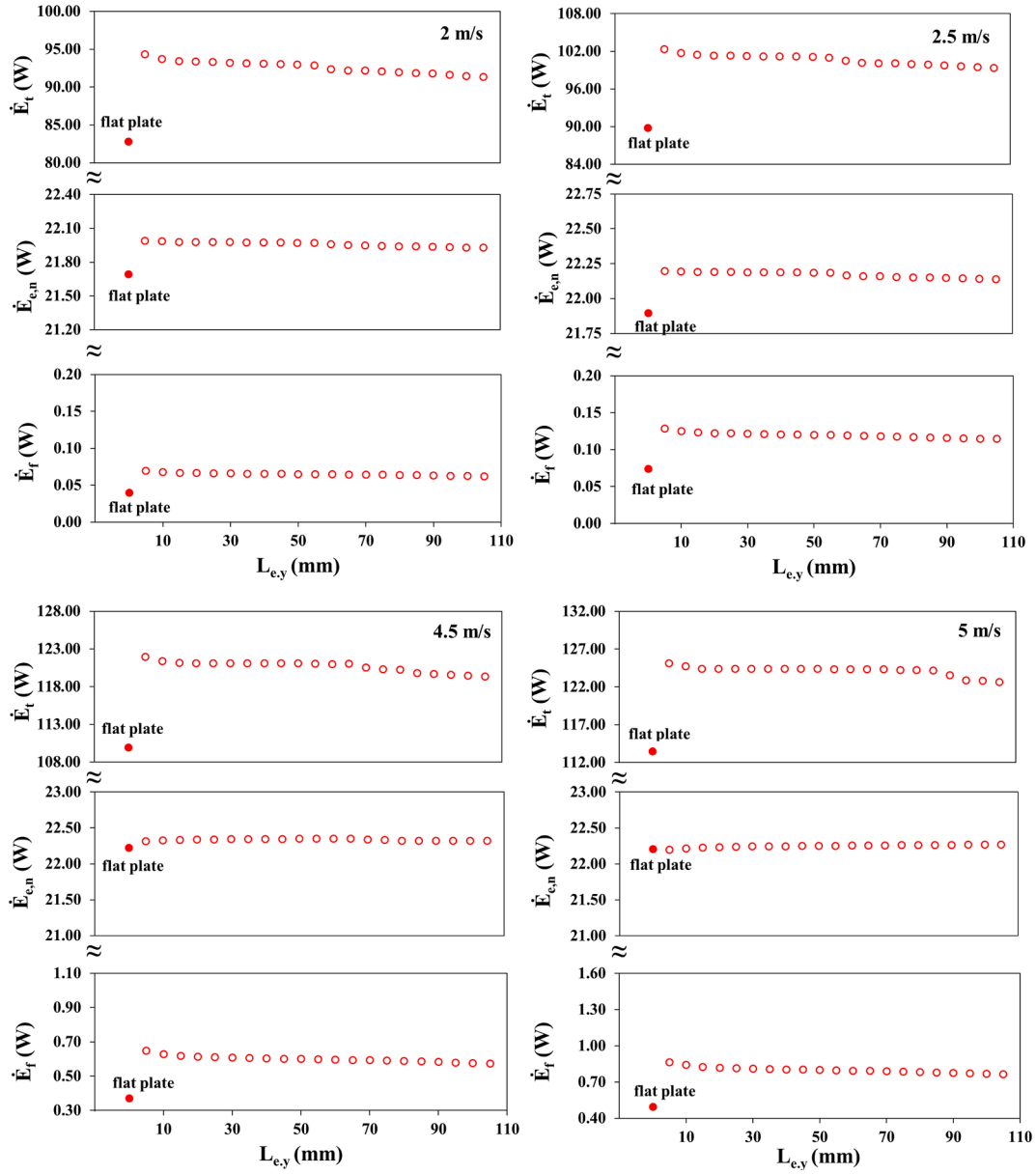

Fig. 11. Variations of $\dot{E}_t$, $\dot{E}_{e,n}$, and $\dot{E}_f$ different $L_{e,y}$ within an inlet velocity range of 2 to 5 m/s.

while showing higher air outlet temperature, highlighted the importance of airfoil placement in enhancing the performance of the PVT collector.

In Figs. 11 and 12, the variations of energy and exergy rates are presented for different $L_{e,y}$ and v_i. Thermal and electrical energy and exergy production are parameters dependent on outlet air temperature and cell temperature, respectively. Therefore, as $L_{e,y}$ changes from 5 mm to 105 mm, thermal energy and exergy rate decrease because of the reduction in outlet air temperature, and the decrease in pressure drop results in a decline in the power consumption of the fan. Use of airfoils improved heat transfer. However, the improvement in heat transfer necessitated additional fan power. For all inlet velocities, an increase in $L_{e,y}$ from 5 mm to 105 mm results in a rise in cell temperature and a decrease in pressure difference. At lower inlet velocities (2 and 2.5 m/s), the impact of changes in cell temperature is more dominant than that of pressure difference. Under these conditions, positioning the airfoils closer to the collector inlet and outlet mouths ($L_{e,y}$) enhances both the electrical energy and the exergy rates. Conversely, at higher inlet velocities (4.5 and 5 m/s), the influence of pressure difference becomes more pronounced than that of cell temperature. For higher inlet velocity operations, suitable airfoil placement, in terms of maximizing electrical energy and exergy rates, is achieved when $L_{e,y}$ is positioned between 55 mm and 70 mm. The net electrical energy and exergy rates are higher than that of the flat plate up to $v_i = 5$ m/s, but almost at the same levels at $v_i = 5$ m/s for base-case conditions in Table 5. The main reason for this is that the increase in electrical energy and exergy obtained is proportionally less than the increase in fan power consumption. Despite achieving the highest thermal energy and exergy production rates for all v_i in arrangements with $L_{e,y} = 5$ mm and 10 mm, the electrical energy and exergy production rates were lower for v_i between 4–5 m/s compared to other arrangements. For airfoils arrangements other than $L_{e,y} = 5$ mm and 10 mm, the inlet velocity upper limit should not exceed 5 m/s for base-case conditions. When it exceeds 5 m/s, the advantage of the airfoils cannot be utilized for net electrical production rate compared to the flat plate. These results underscore the importance of accurately determining operational parameters, such as flow rate, to achieve higher thermal and electrical energy and exergy production in designed PVT collector.

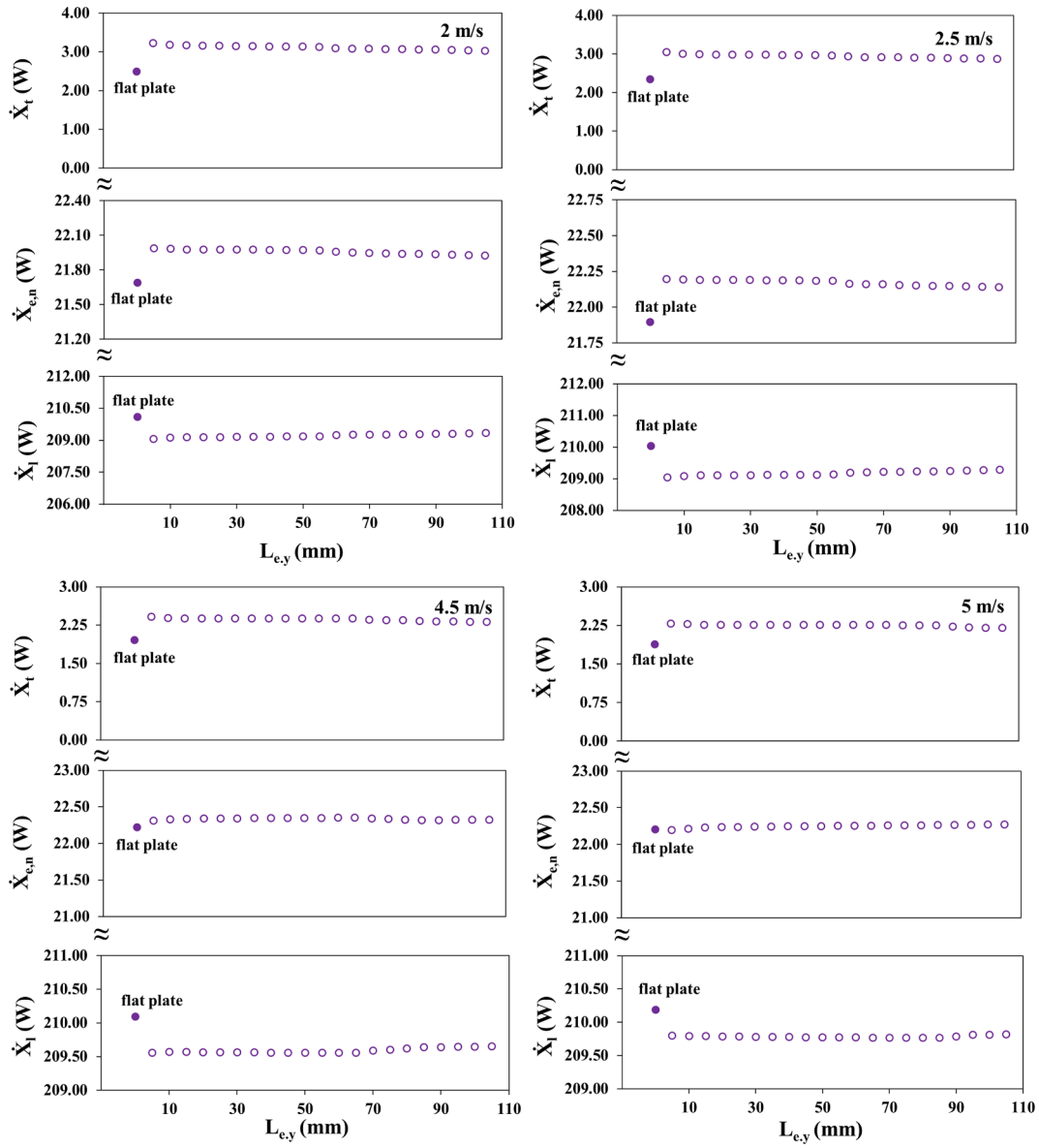

Fig. 12. Variations of $\dot{X}_t$, $\dot{X}_{e,n}$, and $\dot{X}_f$ for different $L_{e,y}$ within an inlet velocity range of 2 to 5 m/s.

The variation in airfoil arrangement from $L_{e,y} = 5$ mm to Le,y = 105 mm resulted in a decrease in all performance metrics, except for electrical efficiency, as illustrated in Figs. 13 and 14. This outcome can be attributed to the deterioration of heat transfer efficiency and the increase in pressure losses. Additionally, it was determined that the difference between the performance parameters, such as electrical energy, primary energy saving, and exergy efficiencies obtained from the flat plate and those obtained from the PVT design diminishes as the flow rate raises. The main cause for this is the significant effect of pressure drop on these performance metrics. Although generally the highest thermal efficiency was obtained at $L_{e,y} = 5$ mm, the lowest electrical efficiency was obtained at $L_{e,y} = 5$ mm, especially for $v_i = 5$ m/s. Considering the influence of inlet air velocity on electrical efficiency under a solar irradiance of 1000 W/m^2, the proposed design is recommended to operate at air velocities not exceeding 5 m/s to maintain its superior performance. Although the fan power consumption remains nearly constant for specified inlet velocities, the net electrical output and, consequently, the electrical efficiency, vary with changes in solar irradiance. This variability necessitates the establishment of different upper inlet velocity limits to sustain superior performance relative to a flat plate PVT collector across different solar irradiance conditions. Table A1 provides the recommended upper inlet velocity thresholds for each performance metric at different solar radiation intensities. Specifically, lower inlet velocity caps are suggested at lower irradiance levels to sustain superior electrical and exergy efficiencies. Meanwhile, for thermal efficiency and primary energy saving efficiency, the PVT system consistently outperforms the flat plate configuration at all tested velocities, obviating the need to define an upper velocity constraint for these criteria. The results demonstrated the importance of accurately positioning the airfoils in the y-direction and determining the appropriate operating conditions for achieving the highest efficiency levels.

3.2. Comparison of NACA 8412 airfoil placement at varying distances in the x-direction ($L_{e,x}$)

In this part, the effects of NACA 8412 model airfoils placed at different distances in the x-direction on the important metrics of the PVT collector were examined. $L_{e,y}$ was set 65 mm, as this value demonstrated consistently favorable outcomes in prior analyses. $L_{e,x}$ was varied at intervals of 5 mm from 5 mm to 65 mm.

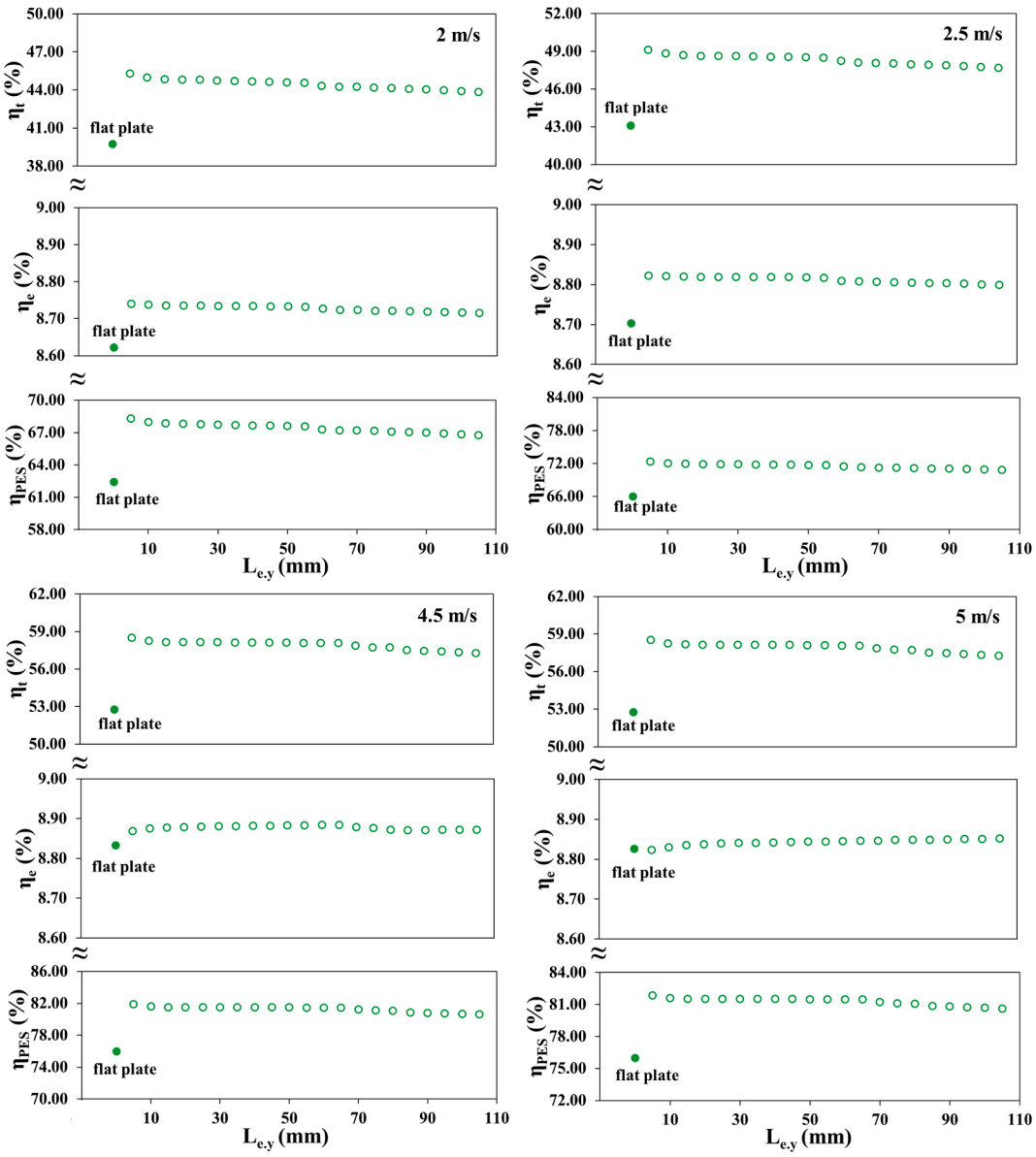

Fig. 13. Variations of η_t, η_e, and η_{PES} for different $L_{e,y}$ within an inlet velocity range of 2 to 5 m/s.

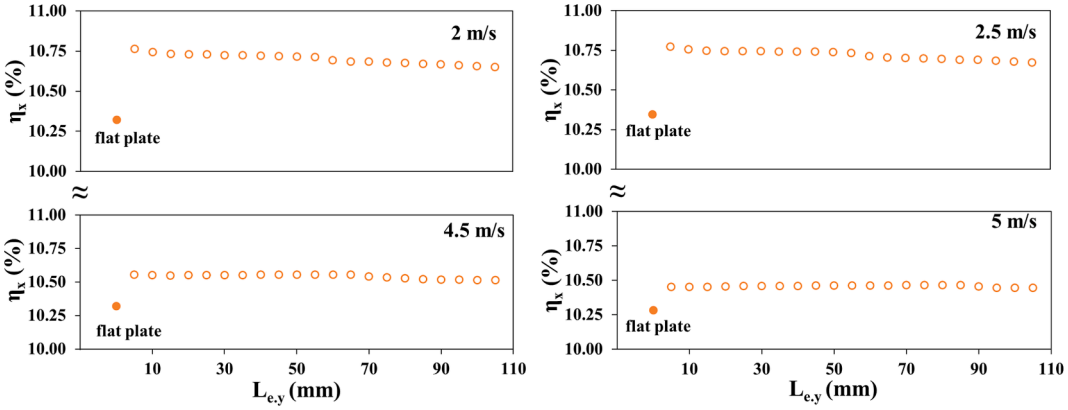

Fig. 14. Variations of η_x for different $L_{e,y}$ within an inlet velocity range of 2 to 5 m/s.

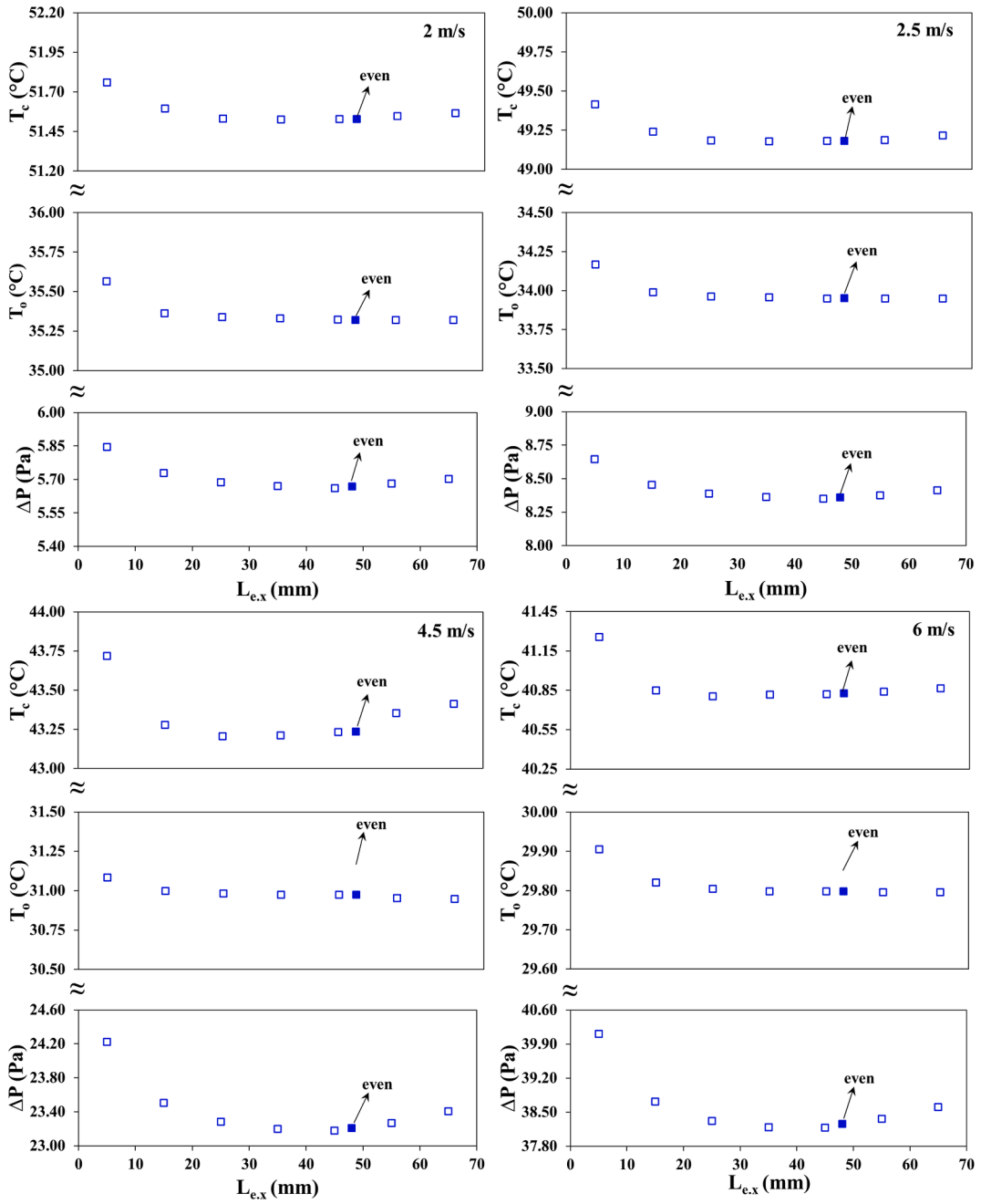

Fig. 15. Variations of T_c, T_o and ΔP for different $L_{e,x}$ within an inlet velocity range of 2 to 6 m/s.

The analysis revealed that the lowest cell temperatures and pressure drops were achieved at $L_{e,x} = 35$ and $L_{e,x} = 45$ (Fig. 15). For $L_{e,x} = 65$, velocity profiles between the airfoil profiles reached their peak values, while the velocity at the right and left margins of the PVT collector for it was lower than in other configurations (Fig. 16-**a**). Moreover, at $L_{e,x} = 35$, velocity distribution within the channel was more uniform compared to $L_{e,x} = 65$, resulting in a more homogeneous temperature distribution along the channel and at the collector outlet (Fig. 16-**b**). This uniform temperature distribution within the channel contributed to a lower average cell temperature (between 40.82 and 51.53 °C) of the PV panel for $L_{e,x} = 35$. The results underscore the significance of both optimal airfoil profile positioning and appropriate determination of operational parameters in enhancing PVT collector performance, as demonstrated by the improved outcomes in air outlet temperature, cell temperature, and pressure drop.

For all flow velocities, the thermal energy production rate reaches its peak at $L_{e,x} = 5$, while the electrical energy production rate predominantly achieves its maximum at $L_{e,x} = 35$ (Fig. 17). Notably, the lowest fan power consumption, corresponding to the lowest pressure drops, is found at $L_{e,x} = 35$ and $L_{e,x} = 45$. The results indicate that the influence of fan power consumption on net electrical energy production must be carefully considered. The trends in thermal and electrical exergy rates closely mirrored those identified in thermal and electrical energy rates (Fig. 18). Although the thermal exergy rates exhibit trends similar to those of thermal energy rates, their numerical values differ significantly. This disparity leads to varying exergy loss trends observed across different inlet velocities. These results highlight the critical importance of accurately determining the x-direction positioning of airfoils to minimize fan power effects and maximize energy and exergy productions in the designed PVT collector.

The highest electrical efficiencies were found at $L_{e,x} = 35$, while the highest thermal and primary energy saving efficiencies were found at L_e,

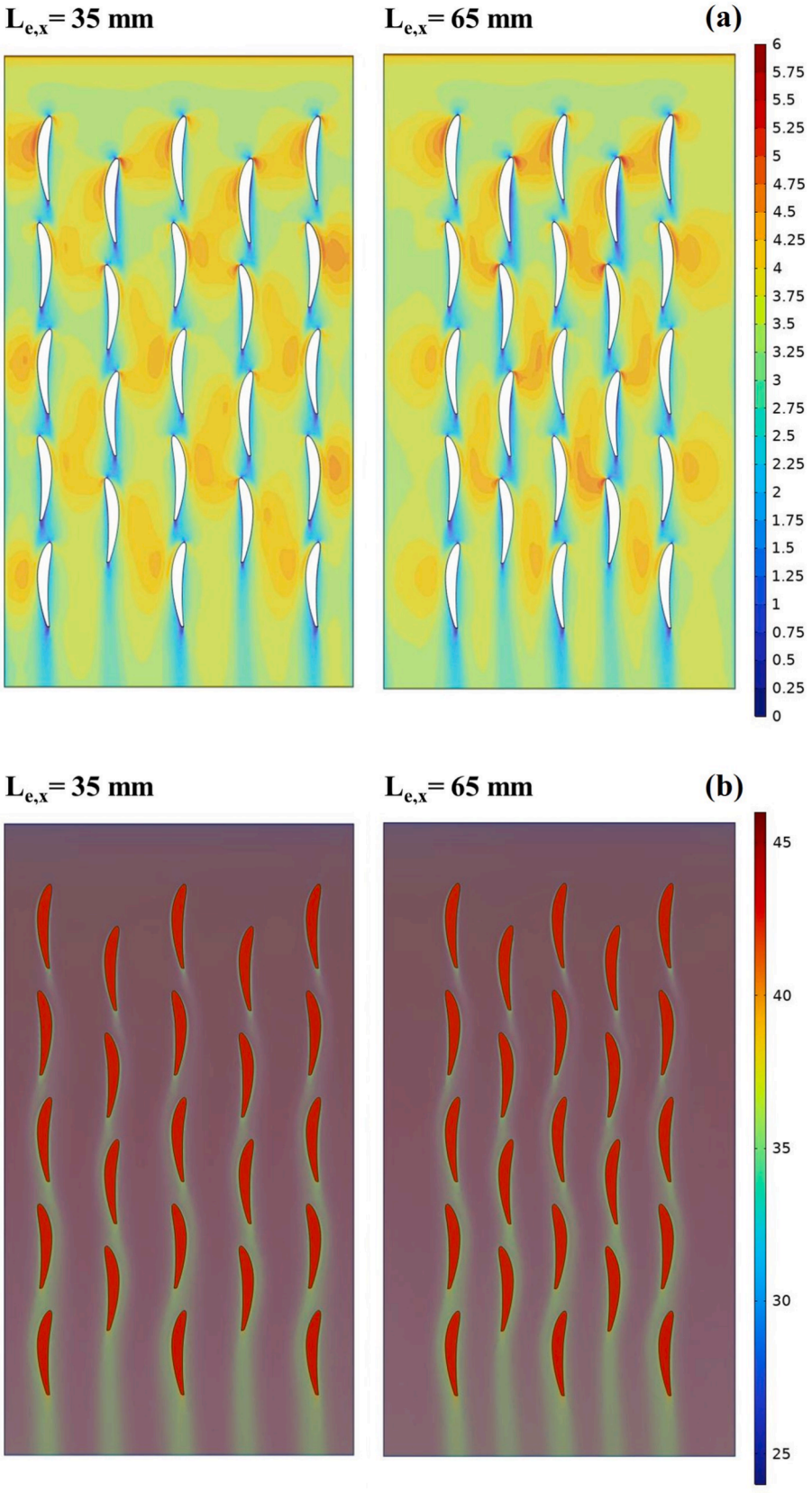

Fig. 16. Velocity (a) and temperature (b) distributions of PVT collectors for different $L_{e,x}$ at v_i = 4.5 m/s.

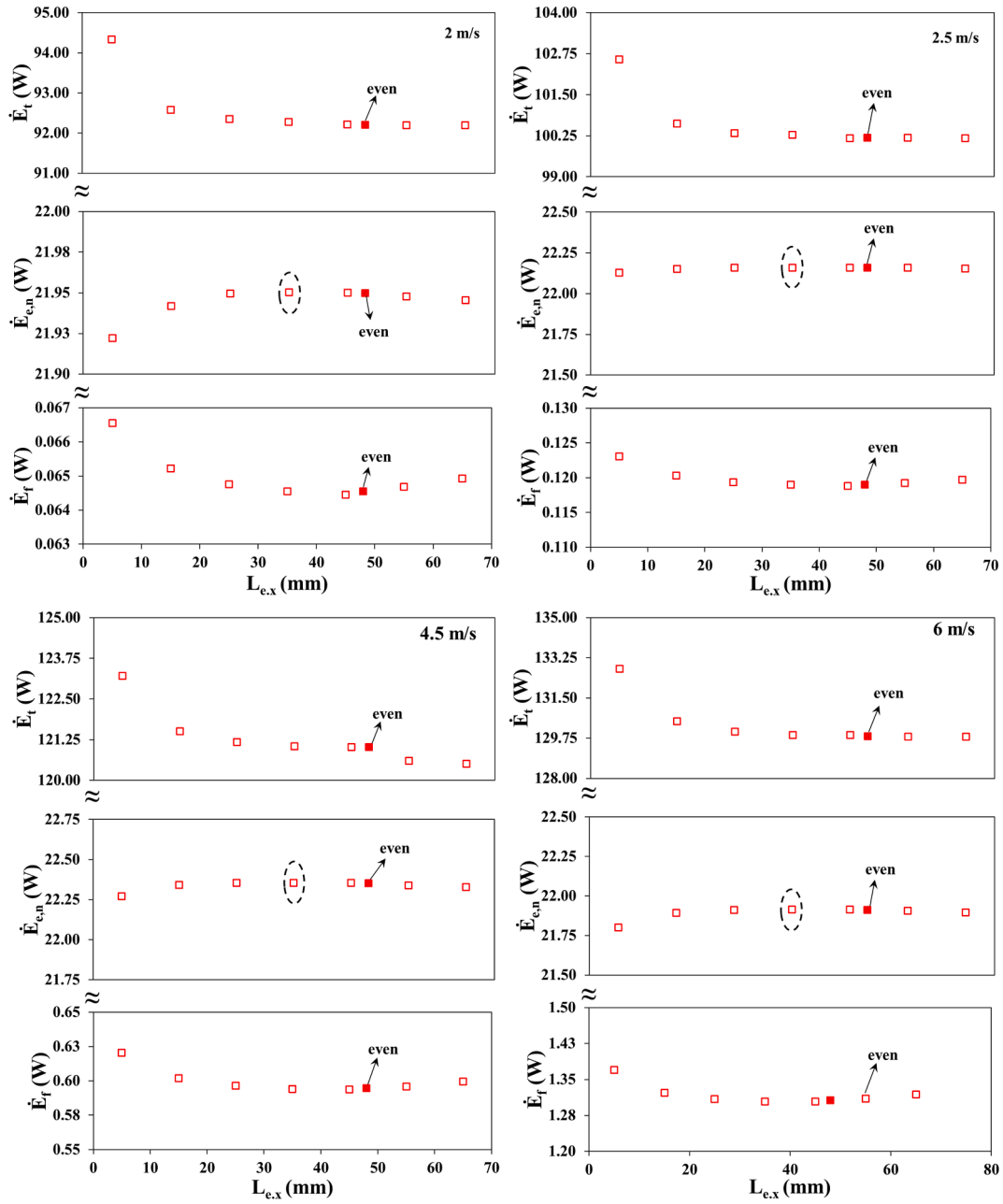

Fig. 17. Variations of $\dot{E}_t$, $\dot{E}_{e,n}$, and $\dot{E}_f$ for different $L_{e,x}$ within an inlet velocity range of 2 to 6 m/s.

$_x = 5$ (Fig. 19). For applications requiring higher thermal power, the airfoil arrangement at $L_{e,x} = 5$ is more suitable, whereas for applications prioritizing higher electrical power, the airfoil arrangement at $L_{e,x} = 35$ is recommended. The maximum exergy efficiency across various airfoil arrangements along the x-direction varied with inlet velocities (Fig. 20). This variation is primarily attributed to differences in the thermal exergy production rate. The airfoil profile arrangement in the x direction can be tailored to meet the specific requirements of various systems. The results of this study are highly significant in guiding such design decisions.

3.3. Economic evaluation

In this study, comprehensive economic analyses were conducted for the proposed PVT collector by considering a range of interest rates and system lifespans across three provinces with distinct climatic conditions. The evaluations focused on three key economic indicators: UAC, $C_{e.n}$, and R_x. Annual net electricity generation and exergy output values specific to the solar potential of each location were utilized in the assessment. The analyses used the NACA airfoil configuration with $L_{e,y} = 65$ mm, $L_{e,x} = 35$ mm, and $v_i = 2$ m/s.

As shown in Table 6, UAC values increase with higher interest rates and decrease with longer system lifespans for all three locations. Among the cases analyzed, the lowest UAC was consistently obtained at a 5 % interest rate and a 20-year lifespan, highlighting the cost-reducing impact of extended operation periods. Similarly, $C_{e.n}$ values tend to decrease as the system lifespan increases but rise with higher interest rates. This trend is observed consistently in Mersin, Muğla, and Trabzon, with Trabzon generally exhibiting higher $C_{e.n}$ values due to its comparatively lower annual energy output. The exergoeconomic performance indicator R_x, representing the exergy output per unit cost, improves with increasing lifespan as a result of declining UAC, while it declines with rising interest rates due to increased cost burdens. In particular, the highest R_x values were recorded at 5 % interest and a 20-year lifespan across all cities.

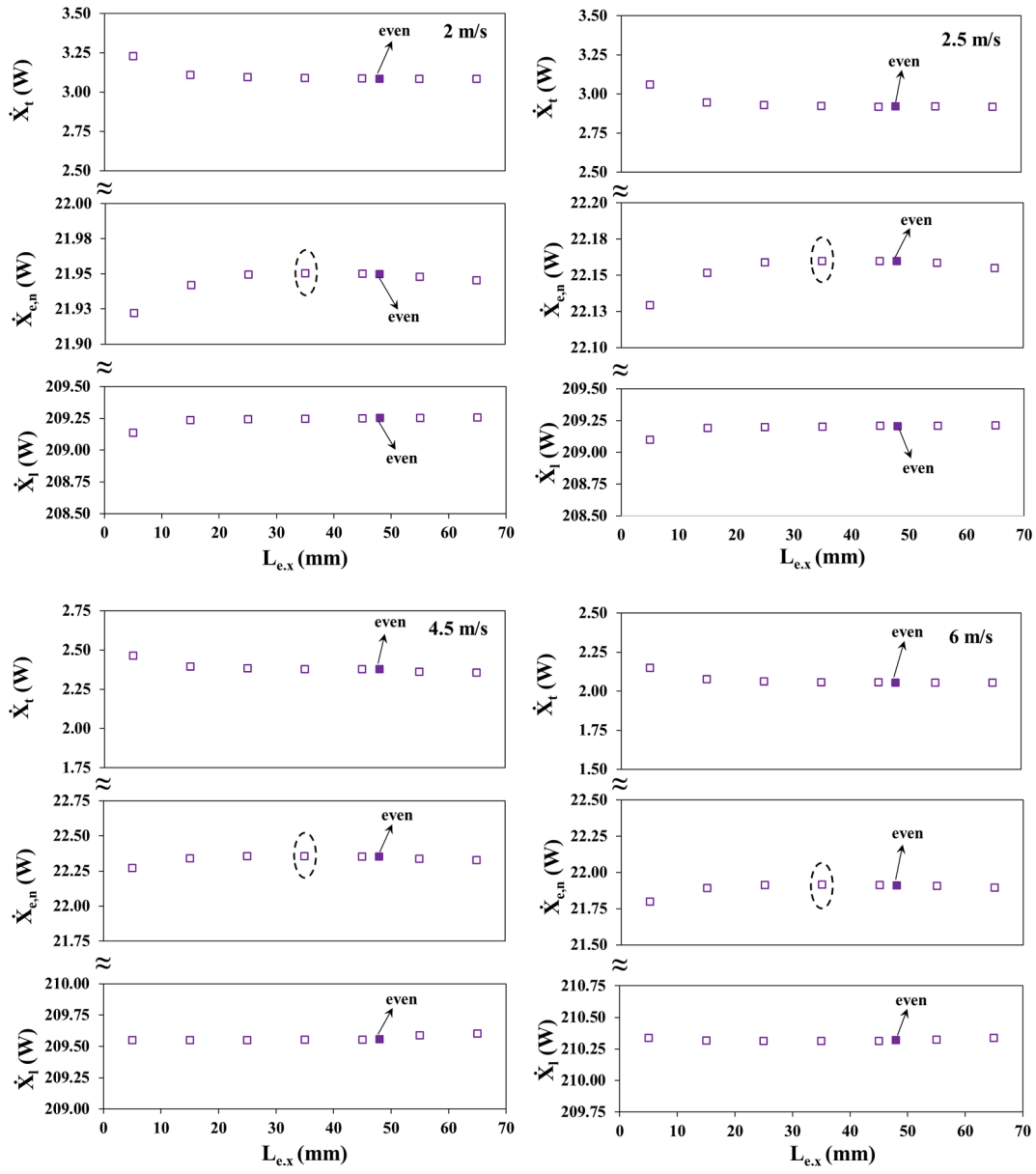

Fig. 18. Variations of $\dot{X}_t$, $\dot{X}_{e,n}$, and $\dot{X}_f$ for different $L_{e,x}$ within an inlet velocity range of 2 to 6 m/s.

These results emphasize the high sensitivity of UAC, $C_{e,n}$, and R_x to both financial parameters and local climatic conditions. Therefore, regional and financial variability should be jointly considered when evaluating the economic feasibility of PVT systems.

3.4. Enviroeconomic evaluation

For the environmental assessment of the presented air-cooled PVT collector, monthly and annual analyses were conducted based on the number of sunny days specific to three provinces in Türkiye. The energy and exergy gains, CO_2 emission reductions, and associated economic savings varied monthly, influenced by local solar irradiation, ambient temperature, and collector efficiency. The analyses used the NACA airfoil configuration with $L_{e,y} = 65$ mm, $L_{e,x} = 35$ mm, and $v_i = 2$ m/s.

As shown in Table 7, the energy-based analysis indicates that regions with higher solar potential, such as Mersin and Muğla, yield greater CO_2 reductions and economic savings compared to regions with lower solar availability, like Trabzon. These values are generally higher during the warmer months, while lower values are observed in colder periods due to reduced solar radiation. Similarly, Table 8 reveals that the exergy-based assessment follows the same trend, with improved environmental and economic performance during summer months and in sunnier regions.

These results highlight the importance of considering both seasonal and regional climatic conditions when evaluating the environmental and economic viability of PVT systems.

3.5. Comparison with literature

Table 9 provides a comparative overview of the electrical, thermal, overall, primary energy saving, and exergy efficiencies of air-cooled PVT collectors equipped with various fin geometries reported in the literature. To facilitate a consistent comparison with the referenced studies, two distinct definitions of electrical efficiency are employed in this study: the first includes the impact of fan power consumption (η_{el}), while the second ($\eta_{el,2}$) excludes it. The values presented in the table reflect the minimum and maximum performance ranges reported under the specific conditions of each referenced work. It is essential to emphasize that

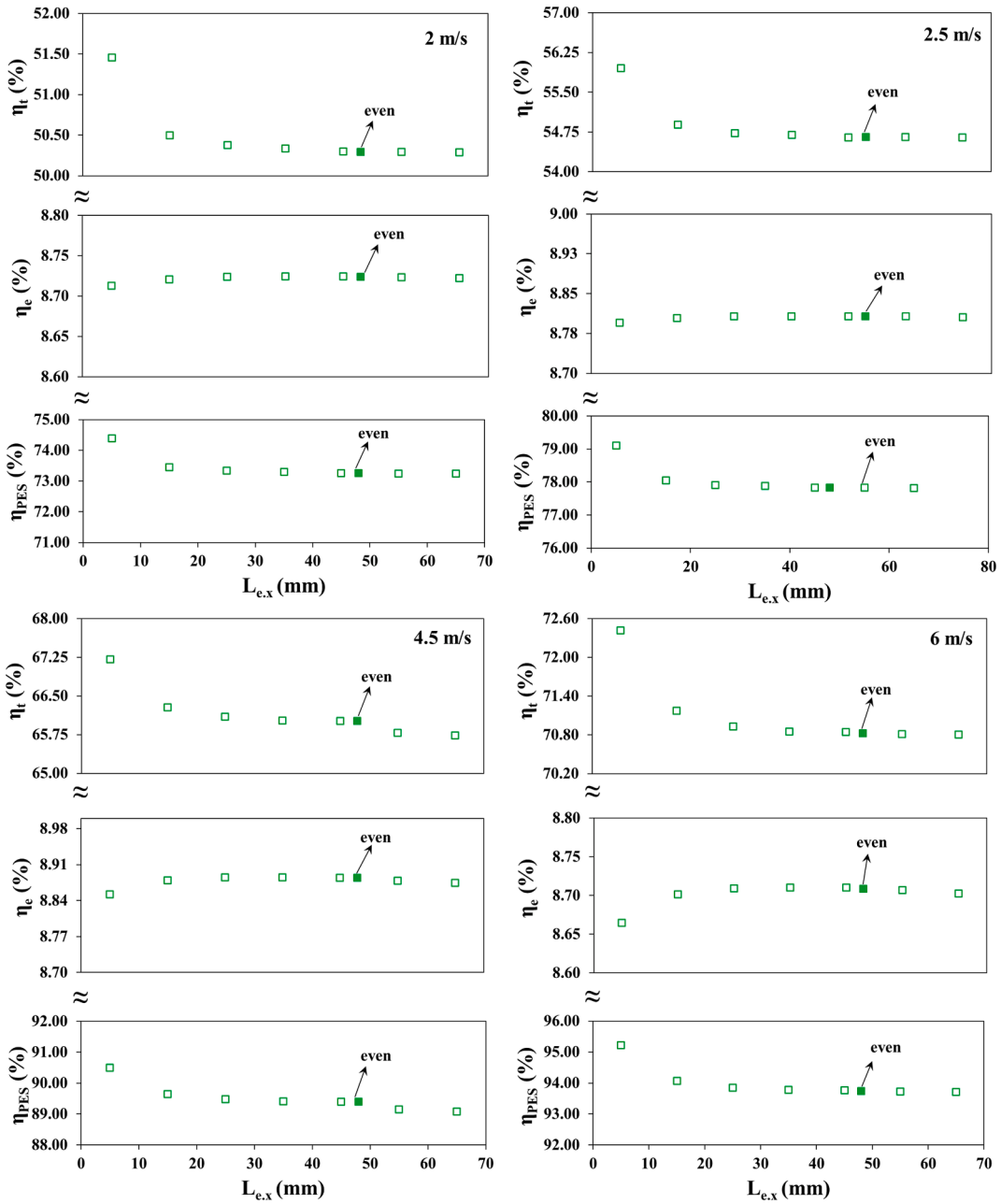

Fig. 19. Variations of η_t, η_e, and η_{PES} for different $L_{e,x}$ within an inlet velocity range of 2 to 6 m/s.

the specific conditions across these studies differ in terms of geometric configurations, ambient and inlet air temperatures, wind speeds, air flow rates, and solar irradiance levels. These variations limit the feasibility of direct, one-to-one performance comparisons.

Nevertheless, the NACA-airfoil configuration examined in the present study exhibits performance values that are not only consistent with but also, in some cases, superior to those of conventional fin designs found in the literature. This comparative evaluation affirms the technical viability and competitive advantage of the NACA 8412 airfoil geometry as an effective enhancement for air-cooled PVT systems.

3.6. Comparison of created ANN model results

The performance of the ANN models was evaluated using Root Mean Square Error (RMSE) and the coefficient of determination (R^2) as key performance indicators to identify the models that provided the most accurate predictions (Fig. 21).

In the first group of ANN models, the third ANN model achieved the highest performance metrics for predicting outlet temperature and pressure drop. Among the ANN models developed for predicting cell temperature in the first group and all outputs in the second group, the fourth ANN model exhibited the highest statistical performance across all evaluation metrics. Specifically, the fourth ANN model in the second group achieved the highest coefficient of determination (R^2) for cell temperature predictions, while the lowest R^2 value was observed for pressure drop predictions.

In Fig. 22, the numerical results of the most effective ANN models for every parameter in Group (1) and Group (2) are compared. The results obtained from the best models of both groups show strong correlation with the numerical findings. The statistical performance indicators for each output parameter in Group (1) surpass those obtained for all output parameters in Group (2). However, the results from Group (2) remain closely aligned with those of Group (1), demonstrating a comparable level of accuracy. Both groups yield acceptable and reliable outcomes,

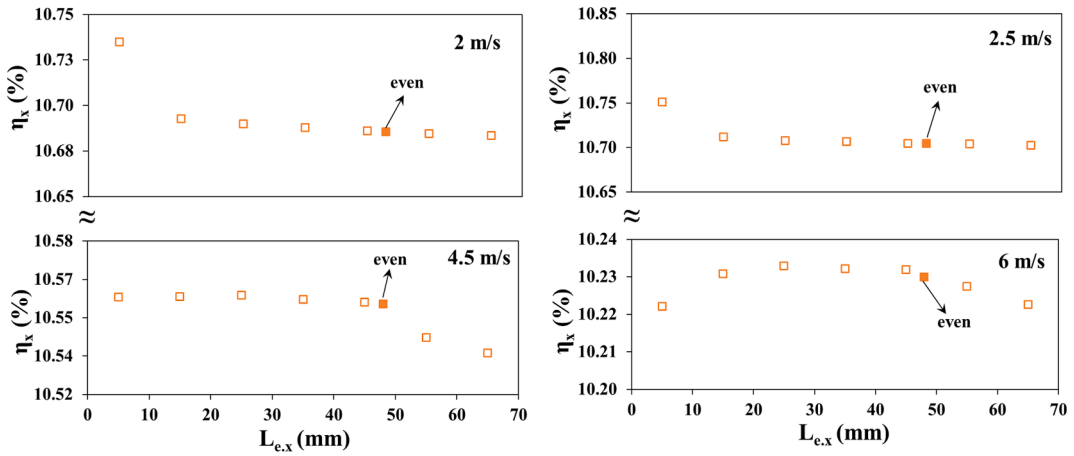

Fig. 20. Variations of η_x for different $L_{e,y}$ within an inlet velocity range of 2 to 6 m/s.

Table 6
Variations in the economical indicators to different interests and lifespans.

P_c ($)	int (%)	n (year)	UAC ($)	$E_{e,n,yearly}$ (kWh/year)	$X_{o\text{-}yearly}$ (kWh/year)	$C_{e,n}$ ($/kWh)			R_x (kWh/$)		
						Me	Mu	Tr	Me	Mu	Tr
88.36	5	10	11.88	Me:47.50	Me:132.17	0.250	0.266	0.348	11.121	10.961	7.871
	10	10	15.26	Mu:44.71	Mu:130.27	0.321	0.341	0.446	8.659	8.535	6.129
	15	10	18.93	Tr:34.19	Tr:93.55	0.398	0.423	0.554	6.982	6.881	4.941
	20	10	22.84			0.481	0.511	0.668	5.786	5.703	4.095
	5	15	8.95			0.188	0.200	0.262	14.760	14.548	10.447
	10	15	12.50			0.263	0.280	0.366	10.573	10.421	7.484
	15	15	16.44			0.346	0.368	0.481	8.041	7.926	5.692
	20	15	20.67			0.435	0.462	0.604	6.396	6.304	4.527
	5	20	7.53			0.158	0.168	0.220	17.548	17.296	12.420
	10	20	11.26			0.237	0.252	0.329	11.736	11.567	8.306
	15	20	15.44			0.325	0.345	0.452	8.559	8.436	6.058
	20	20	19.91			0.419	0.445	0.582	6.638	6.542	4.698

Table 7
Variations in the energy-based enviro-economic indicators from month to year.

Months	N_{days}			$\dot{E}_{en}$ (kWh)			$\varnothing_{CO_2,en}$(tCO_2/month)			$Z_{CO_2,en}$($/month)		
	Me	Mu	Tr	Me	Mu	Tr	Me	Mu	Tr	Me	Mu	Tr
January	20	18	17	15.02	18.10	15.66	0.031	0.038	0.033	0.45	0.55	0.47
February	18	15	16	16.61	14.38	18.72	0.034	0.030	0.040	0.50	0.43	0.56
March	23	20	16	27.17	24.94	20.46	0.056	0.052	0.042	0.82	0.75	0.62
April	23	20	15	31.53	25.10	18.47	0.065	0.052	0.038	0.95	0.76	0.56
May	25	22	17	34.76	28.92	19.13	0.072	0.060	0.040	1.05	0.87	0.58
June	27	25	18	32.14	34.36	21.24	0.067	0.071	0.044	0.97	1.04	0.64
July	30	29	23	38.50	36.36	24.94	0.080	0.076	0.052	1.16	1.10	0.75
August	30	29	21	37.74	36.78	23.03	0.079	0.077	0.048	1.14	1.11	0.69
September	28	26	18	38.23	31.02	17.79	0.080	0.064	0.037	1.15	0.94	0.54
October	26	24	17	32.98	25.75	17.08	0.069	0.054	0.036	0.99	0.78	0.52
November	23	21	18	22.04	20.16	15.24	0.046	0.042	0.032	0.66	0.61	0.46
December	20	17	17	16.29	12.09	9.18	0.034	0.025	0.019	0.49	0.36	0.28
Annual	293	266	213	343.02	307.97	220.93	0.713	0.641	0.460	10.34	9.29	6.66

validating their suitability for practical applications. For scenarios where achieving the highest possible accuracy is paramount, the models developed for individual output parameters in Group (1) are more appropriate. Conversely, if a balance between high accuracy and practical applicability is prioritized, the integrated model proposed for all output parameters in Group (2) is a more suitable choice.

Since the ANN models developed for both groups demonstrated high accuracy, they are expected to offer researchers a practical means for comparing PVT collectors with various fin configurations reported in the literature. Furthermore, these models will facilitate the integration of the designed PVT collector into the dynamic analyses of different processes such as heating, cooling, and drying conducted in the MATLAB or similar computational environments.

Table 8
Variations in the exergy-based enviro-economic indicators from month to year.

Months	N_{days}			$\dot{E}_x$ (kWh)			$\varnothing_{CO_2,x}$(tCO_2/month)			$Z_{CO_2,x}$($/month)		
	Me	Mu	Tr	Me	Mu	Tr	Me	Mu	Tr	Me	Mu	Tr
January	20	18	17	7.29	8.16	5.54	0.015	0.017	0.011	0.22	0.25	0.17
February	18	15	16	7.70	7.46	7.27	0.016	0.016	0.015	0.23	0.22	0.22
March	23	20	16	11.65	12.02	7.84	0.024	0.025	0.016	0.35	0.36	0.24
April	23	20	15	11.66	11.64	7.75	0.024	0.024	0.016	0.35	0.35	0.23
May	25	22	17	12.80	13.01	8.54	0.027	0.027	0.018	0.39	0.39	0.26
June	27	25	18	12.96	12.51	9.25	0.027	0.026	0.019	0.39	0.38	0.28
July	30	29	23	14.46	14.33	11.51	0.030	0.030	0.024	0.44	0.43	0.35
August	30	29	21	14.41	13.90	9.65	0.030	0.029	0.020	0.43	0.42	0.29
September	28	26	18	12.69	12.88	8.10	0.026	0.027	0.017	0.38	0.39	0.24
October	26	24	17	11.19	10.34	6.99	0.023	0.021	0.015	0.34	0.31	0.21
November	23	21	18	8.64	8.21	6.45	0.018	0.017	0.013	0.26	0.25	0.19
December	20	17	17	6.71	5.80	4.65	0.014	0.012	0.009	0.20	0.17	0.14
Annual	293	266	213	132.17	130.27	93.55	0.275	0.271	0.195	3.99	3.93	2.82

Table 9
Comparison of some PVT studies with different fins in the literature and the present PVT collector in terms of performance indicators.

Ref.	Type of fin	Efficiency (%)					
		η_{el}	$\eta_{el,2}$	η_t	η_o	η_{PES}	η_x
[26]	buffles with holes	–	11.66–13.10	24.77–37.40			
[43]	∇-corrugated absorber	–	–	–	–	–	12.89–13.36
[60]	flat transpired				54.29		8.66
[61]	longitudinal fins and rectangular turbulators	–	16.9–17.32	16.9–17.32		79.72–89.52	–
[62]	longitudinal fins		8–9	45–63	–	66.05–86.68	–
[63]	pin fin	–	4.07–4.90	29.14–42.6	33.21–47.50	39.85–55.49	7.27–8.26
[64]	pin fin	–	–	–	–	55.2–61.4	9.60–9.95
Present study	NACA airfoil	8.71–8.90	8.75–9.23	50.34–70.85	59.06–79.56	73.30–93.77	10.23–10.69

Estimated parameter	First Group			Second Group		
	Name of model	RMSE	R^2	Name of model	RMSE	R^2
T_o (°C)	T_o-ANN-1	0.00114838	0.999933	PVT-ANN-1	0.00708676	0.997436
	T_o-ANN-2	0.00090933	0.999958	PVT-ANN-2	0.001753	0.999844
	T_o-ANN-3	0.00064854	0.999979	PVT-ANN-3	0.00126316	0.999919
	T_o-ANN-4	0.00074609	0.999972	**PVT-ANN-4**	0.00085525	0.999963
T_c (°C)	T_c-ANN-1	0.00337806	0.999771	PVT-ANN-1	0.01069621	0.997696
	T_c-ANN-2	0.00295752	0.999824	PVT-ANN-2	0.00325065	0.999788
	T_c-ANN-3	0.00288971	0.999833	PVT-ANN-3	0.00302149	0.999817
	T_c-ANN-4	0.00258741	0.999865	**PVT-ANN-4**	0.00282893	0.999839
ΔP (Pa)	ΔP-ANN-1	0.00323476	0.99995	PVT-ANN-1	0.01732415	0.998553
	ΔP-ANN-2	0.0022343	0.999976	PVT-ANN-2	0.00398668	0.999924
	ΔP-ANN-3	0.0016532	0.999987	PVT-ANN-3	0.00251809	0.999969
	ΔP-ANN-4	0.00190713	0.999982	**PVT-ANN-4**	0.00216675	0.999977

Fig. 21. Performance indicators for developed ANNs.

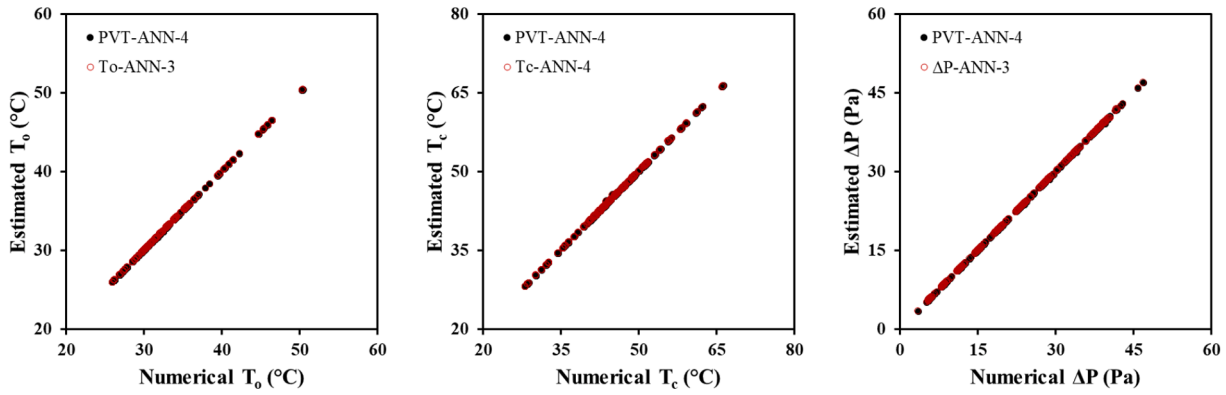

Fig. 22. Comparison of the most effective ANNs.

4. Conclusions

This study presented a numerical performance analysis of an air-cooled PVT collector integrated with NACA 8412 airfoils, focusing on energy, exergy, economic, and environmental aspects, and also developed ANN-based models to predict key output parameters. The key conclusions are:

- For inlet velocities below 4.5 m/s under base-case conditions, $L_{e,y}$ = 5 mm spacing yielded superior thermal and electrical performance, whereas at 4.5 m/s and above, the electrical efficiency declined due to increased pressure losses, reaching levels comparable to or lower than those of flat plate PVT collectors at 5 m/s.
- A favorable x-direction ($L_{e,x}$) spacing was identified at 35 mm, providing lower cell temperatures, reduced pressure drop, and superior electrical and exergy performance.
- Economic analysis showed that longer system lifespans and lower interest rates notably reduce electricity costs and improve exergoeconomic performance. With a single collector, Mersin yielded the most favorable results, achieving the lowest cost of 0.158 $/kWh and the highest R_x value of 17.55 kWh/$, followed by Muğla and Trabzon.
- Environmental analysis revealed that, with a single collector, CO_2 emission reductions and associated savings vary by region and season, with higher values in warmer months and sunnier locations. Mersin and Muğla outperformed Trabzon, with annual reductions in Mersin reaching 0.713 t (energy-based) and 0.275 t (exergy-based), corresponding to savings of $10.34 and $3.99, respectively.
- ANN models developed for both individual and combined output parameters demonstrated high prediction accuracy. The Group (1) model (ANN-3 and ANN-4) achieved the best performance for temperature and pressure prediction, while the Group (2) model offered a balanced, practical solution.

Overall, the integration of NACA 8412 airfoils into PVT collectors provided enhanced energy and exergy efficiencies without excessive pressure penalties at optimal spacing. The study also introduces novel ANN tools and design insights, offering a valuable contribution for future PVT system development and integration.

CRediT authorship contribution statement

Kamil Neyfel Çerçi: Writing – review & editing, Writing – original draft, Visualization, Validation, Methodology, Investigation, Formal analysis, Conceptualization.

Declaration of competing interest

The authors declare that they have no known competing financial interests or personal relationships that could have appeared to influence the work reported in this paper.

Appendix

See Table A1.

Table A1
Recommended inlet velocity upper limits for performance metrics.

Solar radiation (W/m^2)	Upper limits (v_i)			
	η_t	η_e	η_{PES}	η_x
200	no limits	2 m/s	no limits	2 m/s
400	no limits	2.5 m/s	no limits	3.5 m/s
600	no limits	3.5 m/s	no limits	4.5 m/s
800	no limits	4.5 m/s	no limits	5.5 m/s
1000	no limits	5 m/s	no limits	no limits

Appendix A. Supplementary data

Supplementary data to this article can be found online at https://doi.org/10.1016/j.applthermaleng.2025.126955.

Data availability

No data was used for the research described in the article.

References

[1] O.R. Alomar, O.M. Ali, Energy and exergy analysis of hybrid photovoltaic thermal solar system under climatic condition of North Iraq, Case Stud. Therm. Eng. 28 (2021) 101429, https://doi.org/10.1016/j.csite.2021.101429.

[2] S.H. Ali, O.R. Alomar, O.M. Ali, Energetic and exegetic performance analysis of flat plate solar collector under variables heat transfer coefficient and inlet water temperature, Case Stud. Therm. Eng. 28 (2021) 101700, https://doi.org/10.1016/j.csite.2021.101700.

[3] I.F.U. Muzayanah, H.H. Lean, D. Hartono, K.D. Indraswari, R. Partama, Population density and energy consumption: a study in Indonesian provinces, Heliyon 8 (2022) e10634, https://doi.org/10.1016/j.heliyon.2022.e10634.

[4] C. Şirin, J. Goggins, M. Hajdukiewicz, A review on building-integrated photovoltaic/thermal systems for green buildings, Appl Therm Eng 229 (2023) 120607, https://doi.org/10.1016/j.applthermaleng.2023.120607.

[5] M. Kumar, Social, economic, and environmental impacts of renewable energy resources, Wind Solar Hybrid Renewable Energy System (2020).

[6] P. Jha, B. Das, R. Gupta, J.D. Mondol, M.A. Ehyaei, Review of recent research on photovoltaic thermal solar collectors, Sol. Energy 257 (2023) 164–195, https://doi.org/10.1016/j.solener.2023.04.004.

[7] M.Q. Raza, M. Nadarajah, C. Ekanayake, On recent advances in PV output power forecast, Sol. Energy 136 (2016) 125–144, https://doi.org/10.1016/j.solener.2016.06.073.

[8] O.R. Alomar, O.M. Ali, B.M. Ali, V.S. Qader, O.M. Ali, Energy, exergy, economical and environmental analysis of photovoltaic solar panel for fixed, single and dual axis tracking systems: an experimental and theoretical study, Case Stud. Therm. Eng. 51 (2023) 103635, https://doi.org/10.1016/j.csite.2023.103635.

[9] M. Erdiwansyah, R. Mamat, M.S.M. Sani, F. Khoerunnisa, A. Kadarohman, Target and demand for renewable energy across 10 ASEAN countries by 2040, Electr. J. 32 (2019) 106670, https://doi.org/10.1016/j.tej.2019.106670.

[10] O.M. Ali, O.R. Alomar, S.I. Mohamed, Technical, economical and environmental feasibility study of a photovoltaic system under the climatic condition of north Iraq, Int. J. Ambient Energy 44 (2023) 212–220, https://doi.org/10.1080/01430750.2022.2126004.

[11] S. Gorjian, E. Bousi, Ö.E. Özdemir, M. Trommsdorff, N.M. Kumar, A. Anand, K. Kant, S.S. Chopra, Progress and challenges of crop production and electricity generation in agrivoltaic systems using semi-transparent photovoltaic technology, Renew. Sustain. Energy Rev. 158 (2022) 112126, https://doi.org/10.1016/j.rser.2022.112126.

[12] S. Diwania, S. Agrawal, A.S. Siddiqui, S. Singh, Photovoltaic–thermal (PV/T) technology: a comprehensive review on applications and its advancement, Int. J. Energy Environ. Eng. 11 (2020) 33–54, https://doi.org/10.1007/s40095-019-00327-y.

[13] Y. Gao, G. Hu, Y. Zhang, X. Zhang, An experimental study of a hybrid photovoltaic thermal system based on ethanol phase change self-circulation technology: energy and exergy analysis, Energy 238 (2022) 121663, https://doi.org/10.1016/j.energy.2021.121663.

[14] O.M. Hamdoon, O.R. Alomar, B.M. Salim, Performance analysis of hybrid photovoltaic thermal solar system in Iraq climate condition, Therm. Sci. Eng. Prog. 17 (2020) 100359, https://doi.org/10.1016/j.tsep.2019.100359.

[15] Y. Gao, D. Wu, Z. Dai, C. Wang, B. Chen, X. Zhang, A comprehensive review of the current status, developments, and outlooks of heat pipe photovoltaic and photovoltaic/thermal systems, Renew Energy 207 (2023) 539–574, https://doi.org/10.1016/j.renene.2023.03.039.

[16] A.K. Tiwari, K. Chatterjee, S. Agrawal, G.K. Singh, A comprehensive review of photovoltaic-thermal (PVT) technology: performance evaluation and contemporary development, Energy Rep. 10 (2023) 2655–2679, https://doi.org/10.1016/j.egyr.2023.09.043.

[17] S.S. Joshi, A.S. Dhoble, Photovoltaic -thermal systems (PVT): technology review and future trends, Renew. Sustain. Energy Rev. 92 (2018) 848–882, https://doi.org/10.1016/j.rser.2018.04.067.

[18] A.K. Hamzat, A.Z. Sahin, M.I. Omisanya, L.M. Alhems, Advances in PV and PVT cooling technologies: a review, Sustainable Energy Technol. Assess. 47 (2021) 101360, https://doi.org/10.1016/j.seta.2021.101360.

[19] S.M. Sultan, M.N. Ervina Efzan, Review on recent photovoltaic/thermal (PV/T) technology advances and applications, Solar Energy 173 (2018) 939–954.

[20] F. Selimefendigil, C. Şirin, Energy and exergy analysis of a hybrid photovoltaic/thermal-air collector modified with nano-enhanced latent heat thermal energy storage unit, J Energy Storage 45 (2022) 103467, https://doi.org/10.1016/j.est.2021.103467.

[21] E. Arslan, M. Aktaş, Ö.F. Can, Experimental and numerical investigation of a novel photovoltaic thermal (PV/T) collector with the energy and exergy analysis, J Clean Prod 276 (2020) 123255, https://doi.org/10.1016/j.jclepro.2020.123255.

[22] S. Singh, S. Agarwal, G.N. Tiwari, D. Chauhan, Application of genetic algorithm with multi-objective function to improve the efficiency of glazed photovoltaic thermal system for New Delhi (India) climatic condition, Sol. Energy 117 (2015) 153–166, https://doi.org/10.1016/j.solener.2015.04.025.

[23] W. Fan, G. Kokogiannakis, Z. Ma, A multi-objective design optimisation strategy for hybrid photovoltaic thermal collector (PVT)-solar air heater (SAH) systems with fins, Sol. Energy 163 (2018) 315–328, https://doi.org/10.1016/j.solener.2018.02.014.

[24] M. Tahmasbi, M. Siavashi, A.M. Norouzi, M.H. Doranehgard, Thermal and electrical efficiencies enhancement of a solar photovoltaic-thermal/air system (PVT/air) using metal foams, J Taiwan Inst Chem Eng 124 (2021) 276–289, https://doi.org/10.1016/j.jtice.2021.03.045.

[25] A.N. Özakin, F. Kaya, Effect on the exergy of the PVT system of fins added to an air-cooled channel: a study on temperature and air velocity with ANSYS Fluent, Sol. Energy 184 (2019) 561–569, https://doi.org/10.1016/j.solener.2019.03.100.

[26] E. Arslan, Ö. Faruk Can, M. Koşan, M. Demirtaş, B. Aktekeli, M. Aktaş, Numerical and experimental assessment of a photovoltaic thermal collector using variable air volume, Therm. Sci. Eng. Prog. 39 (2023) 101735, https://doi.org/10.1016/j.tsep.2023.101735.

[27] O.R. Alomar, H.M. Abd, M.M. Mohamed Salih, Efficiency enhancement of solar air heater collector by modifying jet impingement with v-corrugated absorber plate, J Energy Storage 55 (2022) 105535, https://doi.org/10.1016/j.est.2022.105535.

[28] O.R. Alomar, M.M.M. Salih, H.M. Abd, Performance analysis of single-pass solar air heater thermal collector with adding porous media and finned plate, Energy Storage 5 (2023), https://doi.org/10.1002/est2.447.

[29] K.N. Çerçi, D.B. Saydam, E. Hürdoğan, C. Ozalp, Experimental investigation and artificial neural networks (ANNs) based prediction of thermal performance of solar air heaters with different surface geometry, Sol. Energy 273 (2024) 112499, https://doi.org/10.1016/j.solener.2024.112499.

[30] H.M. Abd, O.R. Alomar, M.M.M. Salih, Improving the performance of solar air heater using a new model of V-corrugated absorber plate having perforations jets, Int J Energy Res 46 (2022) 8130–8144, https://doi.org/10.1002/er.7715.

[31] E. Alic, M. Das, E.K. Akpinar, Design, manufacturing, numerical analysis and environmental effects of single-pass forced convection solar air collector, J Clean Prod 311 (2021) 127518, https://doi.org/10.1016/j.jclepro.2021.127518.

[32] C. Patel, CFD analysis of artificially roughened solar air heater, Nirma University, 2015.

[33] Y.M. Patel, S.V. Jain, V.J. Lakhera, Thermo-hydraulic performance analysis of a solar air heater roughened with reverse NACA profile ribs, Appl Therm Eng 170 (2020) 114940, https://doi.org/10.1016/j.applthermaleng.2020.114940.

[34] Y.M. Patel, S.V. Jain, V.J. Lakhera, Thermo-hydraulic performance analysis of a solar air heater roughened with discrete reverse NACA profile ribs, Int. J. Therm. Sci. 167 (2021) 107026, https://doi.org/10.1016/j.ijthermalsci.2021.107026.

[35] S. Kumar, R.K. Das, K. Kulkarni, Comparative study of solar air heater (SAH) roughened with transverse ribs of NACA 0020 in forward and reverse direction, Case Stud. Therm. Eng. 34 (2022) 102015, https://doi.org/10.1016/j.csite.2022.102015.

[36] S. Kumar, R.K. Das, K. Kulkarni, T. Alam, S.M. Eldin, Designing of low cost solar air heater equipped with roughness of streamlined cross-section, Case Stud. Therm. Eng. 45 (2023) 102915, https://doi.org/10.1016/j.csite.2023.102915.

[37] C. Shen, Y. Zhang, C. Zhang, J. Pu, S. Wei, Y. Dong, A numerical investigation on optimization of PV/T systems with the field synergy theory, Appl Therm Eng 185 (2021) 116381, https://doi.org/10.1016/j.applthermaleng.2020.116381.

[38] O. Büyükalaca, H.M. Kılıç, U. Olmuş, Y.E. Güzelel, K.N. Çerçi, Numerical investigation and ANN modeling of performance for hexagonal boron nitride-water nanofluid PVT collectors, Therm. Sci. Eng. Prog. 43 (2023) 101997, https://doi.org/10.1016/j.tsep.2023.101997.

[39] S. Houda, R. Belarbi, N. Zemmouri, A CFD Comsol model for simulating complex urban flow, Energy Procedia 139 (2017) 373–378, https://doi.org/10.1016/j.egypro.2017.11.224.

[40] M.T. Erdinc, A.E. Aktas, M.N. Kuru, M. Bilgili, O. Aydin, An optimization study on thermo-hydraulic performance arrays of circular and diamond shaped cross-sections in periodic flow, Int. Commun. Heat Mass Transfer 129 (2021) 105706, https://doi.org/10.1016/j.icheatmasstransfer.2021.105706.

[41] BV, C., OY, C. (1998). COMSOL Multiphysics User's Guide© COPYRIGHT 1998–2010 COMSOL AB., (n.d.).

[42] F. Rubbi, K. Habib, R. Saidur, N. Aslfattahi, S.M. Yahya, L. Das, Performance optimization of a hybrid PV/T solar system using soybean oil/MXene nanofluids as a new class of heat transfer fluids, Sol. Energy 208 (2020) 124–138, https://doi.org/10.1016/j.solener.2020.07.060.

[43] A. Fudholi, M. Zohri, N.S.B. Rukman, N.S. Nazri, M. Mustapha, C.H. Yen, M. Mohammad, K. Sopian, Exergy and sustainability index of photovoltaic thermal (PVT) air collector: a theoretical and experimental study, Renew. Sustain. Energy Rev. 100 (2019) 44–51, https://doi.org/10.1016/j.rser.2018.10.019.

[44] A. Priyam, P. Chand, Thermal and thermohydraulic performance of wavy finned absorber solar air heater, Sol. Energy 130 (2016) 250–259, https://doi.org/10.1016/j.solener.2016.02.030.

[45] M. Ahmadinejad, R. Moosavi, Energy and exergy evaluation of a baffled-nanofluid-based photovoltaic thermal system (PVT), Int J Heat Mass Transf 203 (2023) 123775, https://doi.org/10.1016/j.ijheatmasstransfer.2022.123775.

[46] M.S. Manjunath, K.V. Karanth, N.Y. Sharma, Numerical analysis of the influence of spherical turbulence generators on heat transfer enhancement of flat plate solar air heater, Energy 121 (2017) 616–630, https://doi.org/10.1016/j.energy.2017.01.032.

[47] M. Afrand, A. Shahsavar, P.T. Sardari, K. Sopian, H. Salehipour, Energy and exergy analysis of two novel hybrid solar photovoltaic geothermal energy systems incorporating a building integrated photovoltaic thermal system and an earth air heat exchanger system, Sol. Energy 188 (2019) 83–95, https://doi.org/10.1016/j.solener.2019.05.080.

[48] M. Khaki, A. Shahsavar, S. Khanmohammadi, M. Salmanzadeh, Energy and exergy analysis and multi-objective optimization of an air based building integrated

photovoltaic/thermal (BIPV/T) system, Sol. Energy 158 (2017) 380–395, https://doi.org/10.1016/j.solener.2017.09.056.
[49] M. Al-Damook, Z. Khatir, M. Al Qubeissi, D. Dixon-Hardy, P.J. Heggs, Energy efficient double-pass photovoltaic/thermal air systems using a computational fluid dynamics multi-objective optimisation framework, Appl Therm Eng 194 (2021) 117010, https://doi.org/10.1016/j.applthermaleng.2021.117010.
[50] U. Olmuş, Y.E. Güzelel, K.N. Çerçi, O. Büyükalaca, Numerical analysis and comparison of different serpentine-based photovoltaic-thermal collectors, Renew Energy (2024) 122196, https://doi.org/10.1016/j.renene.2024.122196.
[51] J. Yazdanpanahi, F. Sarhaddi, M. Mahdavi Adeli, Experimental investigation of exergy efficiency of a solar photovoltaic thermal (PVT) water collector based on exergy losses, Solar Energy 118 (2015) 197–208, https://doi.org/10.1016/j.solener.2015.04.038.
[52] A. Malvika, U.C. Arunachala, K. Varun, Sustainable passive cooling strategy for photovoltaic module using burlap fabric-gravity assisted flow: a comparative energy, exergy, economic, and enviroeconomic analysis, Appl Energy 326 (2022) 120036, https://doi.org/10.1016/j.apenergy.2022.120036.
[53] H. Hassan, M.S. Yousef, M.S. Ahmed, M. Fathy, Energy, exergy, environmental, and economic analysis of natural and forced cooling of solar still with porous media, Environ. Sci. Pollut. Res. 27 (2020) 38221–38240, https://doi.org/10.1007/s11356-020-09995-4.
[54] M. Emam, A. Hamada, H.A. Refaey, M. Moawed, M.A. Abdelrahman, M.R. Rashed, Year-round experimental analysis of a water-based PVT-PCM hybrid system: comprehensive 4E assessments, Renew Energy 226 (2024), https://doi.org/10.1016/j.renene.2024.120354.
[55] A.A. Al-Ugla, M.A.I. El-Shaarawi, S.A.M. Said, A.M. Al-Qutub, Techno-economic analysis of solar-assisted air-conditioning systems for commercial buildings in Saudi Arabia, Renew. Sustain. Energy Rev. 54 (2016) 1301–1310, https://doi.org/10.1016/j.rser.2015.10.047.
[56] Turkish State Meteorological Service, Statistical Data on Provinces and Districts, [Online]. Available: https://www.mgm.gov.tr/veridegerlendirme/il-ve-ilceler-istatistik.aspx?k=undefined&m. [Accessed: 20-Apr-2025].
[57] H.N.S. Yassien, O.R. Alomar, M.M.M. Salih, Performance analysis of triple-pass solar air heater system: effects of adding a net of tubes below absorber surface, Sol. Energy 207 (2020) 813–824, https://doi.org/10.1016/j.solener.2020.07.041.
[58] O.M. Ali, O.R. Alomar, Technical and economic feasibility analysis of a PV grid-connected system installed on a university campus in Iraq, Environ. Sci. Pollut. Res. 30 (2022) 15145–15157, https://doi.org/10.1007/s11356-022-23199-y.
[59] A. Tiwari, M.S. Sodha, A. Chandra, J.C. Joshi, Performance evaluation of photovoltaic thermal solar air collector for composite climate of India, Sol. Energy Mater. Sol. Cells 90 (2006) 175–189, https://doi.org/10.1016/j.solmat.2005.03.002.
[60] M. Gholampour, M. Ameri, Energy and exergy analyses of photovoltaic/thermal flat transpired collectors: experimental and theoretical study, Appl Energy 164 (2016) 837–856, https://doi.org/10.1016/j.apenergy.2015.12.042.
[61] S.-B. Kim, K.-A. Moon, B.-H. An, K.-H. Choi, H.-U. Choi, Experimental performance evaluation of air-based photovoltaic–thermal collector with rectangular turbulators and longitudinal fins, Energy Rep. 12 (2024) 1315–1324, https://doi.org/10.1016/j.egyr.2024.07.038.
[62] W. Fan, G. Kokogiannakis, Z. Ma, P. Cooper, Development of a dynamic model for a hybrid photovoltaic thermal collector – solar air heater with fins, Renew Energy 101 (2017) 816–834, https://doi.org/10.1016/j.renene.2016.09.039.
[63] M. Huang, Y. Wang, M. Li, V. Keovisar, X. Li, D. Kong, Q. Yu, Comparative study on energy and exergy properties of solar photovoltaic/thermal air collector based on amorphous silicon cells, Appl Therm Eng 185 (2021) 116376, https://doi.org/10.1016/j.applthermaleng.2020.116376.
[64] D. Kong, Y. Wang, M. Li, J. Liang, Experimental investigation of a novel hybrid drying system powered by a solar photovoltaic/thermal air collector and wind turbine, Renew Energy 194 (2022) 705–718, https://doi.org/10.1016/j.renene.2022.05.102.
[65] OneBuilding.org, Climate Data for Turkey – WMO Region 6 Europe. httpssh://climate.onebuilding.org/WMO_Region_6_Europe/TUR_Turkiye (accessed 20 April 2025).